

# Impedance MPC with Patient-Torque Estimation for Knee Rehabilitation Exoskeletons

Yongyan Cao and Jinshan Tang

**Abstract**—Knee rehabilitation exoskeletons must enforce a prescribed joint trajectory while remaining safely compliant with involuntary spasm and voluntary patient effort—objectives in tension for any fixed-gain impedance controller. We present an Impedance Model Predictive Control (Impedance MPC) framework for knee rehabilitation exoskeletons, demonstrated on a series-elastic-actuator (SEA) platform: an algebraic feedforward reduces the knee dynamics to a constant-coefficient scalar double integrator, and a receding-horizon quadratic program (QP) computes corrective torques while enforcing hard range-of-motion, torque, and velocity limits (ISO 13482). A Kalman disturbance state driven by direct SEA-based torque sensing (the series-elastic spring deflection  $k_s\delta$  measured through the elastic element—an intrinsic, EMG-free patient-torque estimate, not a separate load cell) gives a nominal offset-free guarantee (for constant or slowly-varying disturbances, under observability and recursive-feasibility assumptions; Section IV-C) and, via its sign and the desired-motion direction, sensorless Assist-as-Needed. The constant state matrix permits offline precomputation of the QP cost inverse, enabling 500 Hz operation with a 20-step horizon. Across seven-controller benchmarks (sinusoidal tracking, isometric hold), the 500 Hz Kalman MPC is offset-free—0.1 mrad RMS, 0.1 mrad steady-state, 0.2 mrad peak under 15 Nm spasm, versus a 515 mrad steady-state offset for classical impedance at the same stiffness—the direct-measurement channel converging the estimate near-immediately (within a few sampling periods). Without the estimator it realizes a classical impedance (4.8 mrad RMS, 8.3 mrad steady-state). All MPC variants meet the  $\pm 87$  mrad ( $5^\circ$ ) clinical criterion; no classical controller does. The architecture is formulated for the 20-DOF MyoSuite myoLeg via coupling-aware per-joint QPs (an analytical projection from the validated single joint; full closed-loop myoLeg validation is future work).

**Index Terms**—Knee rehabilitation, exoskeleton, impedance control, model predictive control, Kalman filter, patient-torque estimation, joint torque sensing, series elastic actuator, assist-as-needed, disturbance rejection, ISO 13482, MyoSuite, MuJoCo.

## I. INTRODUCTION

**K**NEE rehabilitation after anterior cruciate ligament (ACL) reconstruction, total knee arthroplasty (TKA), or neurological injury requires an exoskeleton that both guides the joint through a prescribed motion and responds gracefully to unpredictable muscular output: early recovery involves high-amplitude involuntary spasm the robot must resist without escalating into a force duel, while later phases require it to yield proportionally to voluntary effort to maximize neuroplasticity [1], [2].

Classical impedance control [3] cannot reconcile these objectives: stiff impedance tracks accurately but, under a spasm  $\tau_{\text{ext}} = 15$  Nm at  $K_d = 30$  Nm/rad, yields a steady-state error  $e_\infty = \tau_{\text{ext}}/K_d = 500$  mrad  $\approx 29^\circ$ , far beyond the  $\pm 5^\circ$  clinical tolerance—and raising  $K_d$  cuts the error only by increasing contact force on a recovering joint. Admittance control [5] yields to patient force, correct for active exercise but wrong for passive stretching, where a spasm must not deflect the trajectory. The market-leading Lokomat resolves this only through a therapist-set compliance that cannot adapt in real time to spasm onset or fatigue [4].

Model Predictive Control (MPC) can resolve both objectives—predictive look-ahead enforces constraints before violation, and a Kalman disturbance state drives steady-state error toward zero without integral windup [6]—but existing rehabilitation impedance-MPC either optimizes impedance *parameters* (nonlinear in the prediction model, limiting updates to 10–30 Hz [7], [8]) or does not propagate the disturbance estimate through the horizon, leaving a residual offset [9].

This paper addresses these limitations with the following contributions:

- 1) **Algebraic feedforward to constant- $A_d$  structure** (Section IV): an algebraic feedforward cancels the actuator and limb inertia and damping (an SEA in the demonstrated platform), leaving a scalar double integrator with a *constant* state matrix  $A_d$ , so the QP cost inverse  $H^{-1}$  is precomputed once offline and the online step is a matrix–vector multiply—enabling 500 Hz operation with  $N = 20$  horizon steps.
- 2) **SEA-based-sensing Kalman patient-torque augmentation** (Section IV-C): direct SEA-based (intrinsic) torque sensing—the spring deflection  $\delta = \theta_m/N - q$  giving a torque estimate  $\hat{\tau}_{\text{ext}} = k_s\delta$  through the *elastic element* (no EMG, no 6-axis load cell), or an accelerometer Newton-residual—drives an integrating Kalman state propagated through all  $N$  steps, cutting steady-state error from 8.3 to 0.1 mrad with a near-zero transient (convergence within a few sampling periods).
- 3) **Sensorless Assist-as-Needed via disturbance sign** (Section V-C):  $\text{sgn}(\dot{d})$  together with the desired-motion direction distinguishes resisting spasm from voluntary effort, scheduling virtual stiffness without EMG or a separate intent-detection subsystem.
- 4) **ROM/torque/velocity constraint embedding** (Section V-A): joint ROM ( $0^\circ$ – $120^\circ$ ), actuator-torque, and velocity limits appear as hard QP inequalities (ISO 13482 [10]) rather than post-hoc saturation, enforced at every predicted step while the QP is feasible.

Manuscript submitted June 2026.

Y. Cao and J. Tang are with the Department of Biomedical Engineering and Engineering Science. Corresponding author: Y. Cao (e-mail: yongyan-cao@gmail.com).

- 5) **Seven-controller benchmarks** (Sections VI–VII): sinusoidal tracking under step spasm and precision isometric hold quantify each design element—all MPC variants meet the 87 mrad (5°) clinical advance criterion, and 500 Hz lowers the no-Kalman contact RMS relative to 100 Hz ( $\approx 8$  vs. 25 mrad).
- 6) **MyoSuite myoLeg extension** (Section VIII): per-joint Impedance MPC with coupling-aware torque bounds is formulated for the 20-DOF myoLeg without a full musculoskeletal model—presented as an analytical projection from the single-joint results (the unloaded gait lower bounds are numerically verified; full closed-loop myoLeg simulation is future work).

## II. RELATED WORK

### A. Impedance MPC for Human–Robot Interaction

Cao, Cheng, and Li [7] optimize impedance *parameters*  $\{M_d, D_d\}$  over a receding horizon with a virtual energy tank for passivity, but the parameters enter the propagation matrices nonlinearly, limiting updates to 10–30 Hz. Here the decision variables are corrective *torques*  $\mathbf{U} \in \mathbb{R}^N$  and the feedforward yields a constant  $A_d$ , enabling offline  $H^{-1}$  precomputation and a 15–50 $\times$  rate advantage; the energy-tank constraint is adopted from [7]. Haninger et al. [8] co-optimize a force reference and impedance changes via stochastic MPC with Gaussian-Process-learned forces and a probabilistic chance constraint; this work instead uses a two-parameter analytic SEA model with a hard, deterministic ISO-13482 bound and a Kalman state that is offset-free in the nominal limit.

Wu et al. [9] pair a model-predictive impedance controller with an ADRC/ESO that compensates the disturbance only at the current step; here the Kalman state is propagated through all  $N$  horizon steps, pre-loading correction before the spasm develops (onset peak 0.2 vs. 8–25 mrad). Reinforcement learning has also been applied to variable-impedance pHRI [18] but requires demonstrations and gives no hard-constraint certificate.

The constant- $A_d$  offset-free architecture was first developed for a redundant manipulator [33]; this paper specializes it to the single-DOF SEA knee—the operational-space inertia collapses to the scalar  $I_{\text{eff}}$ , the disturbance channel becomes the direct spring-deflection measurement  $k_s \delta$ , and the disturbance sign is repurposed for sensorless AAN, an interpretation specific to the bidirectional patient-effort setting.

### B. Knee Rehabilitation Control

The clinically-deployed Lokomat [11] uses an impedance overlay on a position-controlled cable drive with therapist-set stiffness  $K_d \in [5, 50]$  Nm/rad; at  $K_d = 30$  a 15 Nm spasm implies a  $\tau_h/K_d = 500$  mrad equivalent offset (a computed equivalent, not a measured datum)—eliminated here by enforcing the torque limit as a hard QP constraint independent of tracking stiffness. Freeman et al. [12] apply iterative learning control to post-TKA rehabilitation, converging across trials but unable to react within a trial to spasm onset (reflex forces escalate over tens of milliseconds), whereas this framework acts within 2–4 ms at 500 Hz. Riener et al. [13] formalized

patient-cooperative, Assist-as-Needed control—the robot supplying only the deficit torque—motivating the AAN extension of Section V-C.

Fang et al. [27] use a sliding-mode controller with a perturbation observer (SMC-SPO), reaching 3.84 mrad RMSE under a 5 Nm *sinusoidal* disturbance; like the Kalman state it estimates and feeds forward a lumped disturbance, but the MPC additionally (i) propagates  $\hat{d}$  through the horizon, limiting onset/release peaks where SMC must re-capture the sliding surface, (ii) enforces hard ROM/torque limits with feasibility certificates, and (iii) yields sensorless AAN from  $\text{sgn}(\hat{d})$ ; a matched comparison (15 Nm step) is in Section VII-D and Table VIII. Hogan’s impedance formulation [3], Pratt and Williamson’s SEA concept [14], ISO 13482:2014 [10], and the force-control survey [15] underpin Sections III–V.

## III. SYSTEM DYNAMICS

### A. SEA-Driven Knee Joint

1) *Motor-Side Equation of Motion*: The exoskeleton actuator consists of a brushless motor driving the knee through a gearbox of ratio  $N$  with a compliant series spring of stiffness  $k_s$  inserted between the gearbox output shaft and the human-interface link. The motor-side equation is

$$J_m \ddot{\theta}_m + B_m \dot{\theta}_m = \tau_m - \frac{\tau_r}{N} \quad (1)$$

where  $\theta_m$  is the motor rotor angle (rad);  $J_m$  is the combined motor-plus-gearbox inertia ( $\text{kg m}^2$ );  $B_m$  is the viscous damping coefficient of the motor shaft ( $\text{Nm s/rad}$ );  $\tau_m$  is the electromagnetic torque produced by the field-oriented current controller (the control input); and  $\tau_r = k_s(\theta_m/N - q)$  is the spring torque transmitted to the human limb (Nm).

2) *Human-Interface Equation of Motion*: The spring torque drives the combined robot output link and patient shank-foot segment:

$$(J_{\text{robot}} + J_{\text{limb}})\ddot{q} + (B_{\text{robot}} + B_{\text{limb}})\dot{q} = \tau_r + \tau_h(t) + \tau_g(q) \quad (2)$$

where  $q$  is the knee joint angle (rad, measured positive in flexion);  $J_{\text{limb}} \approx 0.446 \text{ kg m}^2$  is the shank-foot inertia about the knee axis (de Leva [16] for a 75 kg, 1.75 m adult; computed as  $I_{\text{shank/knee}} + I_{\text{foot/knee}} = 0.181 + 0.265 \text{ kg m}^2$ , detailed in Section III-A.3);  $B_{\text{limb}}$  is the combined joint viscous damping;  $\tau_h(t)$  is the net patient interaction torque (Nm, the disturbance); and  $\tau_g(q) = -m_{\text{limb}} g L_{\text{cm}} \cos(\alpha + q)$  accounts for the gravitational moment of the shank-foot segment at angle  $q$  (this term is cancelled by the feedforward of Section IV-A).

3) *Simplified Single-Mass Model*: The exoskeleton closes a high-rate inner force loop on the spring deflection [14], so the outer Impedance MPC sees the SEA *output torque* directly and the open-loop spring dynamics are subsumed by that inner loop. The relevant open-loop check is then that the SEA mechanical resonance lies above the rehabilitation *movement* band. With  $k_s = 200 \text{ Nm/rad}$  (joint side),  $N = 80$ ,  $J_m = 1.5 \times 10^{-4} \text{ kg m}^2$ , the spring stiffness reflected to the motor is  $k_s/N^2$ , giving a motor–spring resonance  $\sqrt{k_s/(N^2 J_m)} \approx 14 \text{ rad/s}$  and a coupled two-mass resonance

$\sqrt{k_s(J_{\text{load}}^{-1} + (N^2 J_m)^{-1})} \approx 26 \text{ rad/s} (\approx 4 \text{ Hz})$ . This is well above the  $\leq 0.5 \text{ Hz}$  rehabilitation movement band, so within the task bandwidth the spring is effectively rigid and the two-mass system is well approximated by the single effective mass of (3). The separation is modest in *open loop* ( $\approx 4 \text{ Hz}$  vs.  $0.5 \text{ Hz}$ ,  $\approx 8:1$ ), which is why the architecture does not rely on it directly: the high-rate inner torque loop—whose closed-loop bandwidth (typically 20–50 Hz for SEA force control [14]) exceeds the rehabilitation motion bandwidth by an order of magnitude and actively damps the lightly-damped spring resonance—presents a near-rigid SEA *output torque* to the MPC, and any residual two-mass dynamics above a few Hz are absorbed by the unmodeled-disturbance Kalman channel of Section IV-C. The feedforward of Section IV-A cancels the known gravity torque  $\tau_g(q)$  at the hardware command level; equation (3) therefore represents the **gravity-compensated residual plant** seen by the MPC layer:

$$I_{\text{eff}} \ddot{q} + b_{\text{eff}} \dot{q} = \tau_m^{\text{eff}} + \tau_h(t) \quad (3)$$

where  $I_{\text{eff}} = J_{\text{robot}} + J_{\text{limb}} \approx 0.45 \text{ kg m}^2$ ,  $b_{\text{eff}} = B_{\text{robot}} + B_{\text{limb}} \approx 0.50 \text{ Nm s/rad}$ , and  $\tau_m^{\text{eff}}$  is the torque command referred to the joint output (the control input). The limb inertia  $J_{\text{limb}}$  is computed from de Leva [16] segment tables for a 75 kg adult (height 1.75 m): shank mass  $m_s = 3.49 \text{ kg}$ , radius of gyration  $r_s = 0.130 \text{ m}$ , distance from knee to shank CoM  $d_s = 0.187 \text{ m}$ , giving  $I_{\text{shank/knee}} = m_s(r_s^2 + d_s^2) = 0.181 \text{ kg m}^2$ ; foot mass  $m_f = 1.09 \text{ kg}$ , distance from knee to foot CoM  $d_f \approx 0.488 \text{ m}$ , giving  $I_{\text{foot/knee}} \approx 0.265 \text{ kg m}^2$ ; total  $J_{\text{limb}} \approx 0.446 \text{ kg m}^2$ . Adding the robot output-link inertia  $J_{\text{robot}} \approx 0.005 \text{ kg m}^2$  gives  $I_{\text{eff}} \approx 0.45 \text{ kg m}^2$ . The identification of  $I_{\text{eff}}$  is refined per-session from the first 2–3 minutes of low-amplitude perturbation trials using the spring-deflection measurement channel of Section III-C.

4) *Single-Joint Simulation Benchmark Model*: No open-source single-DOF knee rehabilitation benchmark exists in MuJoCo or OpenSim. Sections VI–VII therefore use a custom MuJoCo knee-pendulum model (`knee_rehab_1dof.xml`) consisting of a fixed thigh body, a shank-foot body connected by a hinge joint at the knee, and a direct-torque actuator (representing the SEA output after inner force-control closure). Shank and foot geometries are cylinders and boxes whose mass and CoM positions match the de Leva [16] parameters quoted above; the resulting  $I_{\text{eff}} \approx 0.45 \text{ kg m}^2$  and  $b_{\text{eff}} = 0.50 \text{ Nm s/rad}$  are verified by comparing the model’s open-loop step-torque response with the analytic prediction of (3). The model file is included as supplementary material (Section IX).

5) *Joint Range-of-Motion*: The normal knee flexion–extension range is  $q \in [0^\circ, 120^\circ] = [0, 2.094] \text{ rad}$ . ISO 13482 [10] requires hardware end-stops and software ROM limits that the control layer must enforce independently. The MPC ROM constraints (Section V-A) provide the software limit with a predictive safety margin that prevents the joint from approaching the hardware end-stop at high velocity.

TABLE I  
SIGN CONVENTIONS

Quantity	Positive value means
$q, \dot{q}$	knee <b>flexion</b> (angle / velocity), anatomical
$\tau_h$	patient torque in the <b>flexion</b> direction, anatomical (enters the limb Newton equation (2))
$d = -\tau_h/I_{\text{eff}}$	the disturbance as it enters the error dynamics (10); $d > 0 \Leftrightarrow$ extension-direction patient torque
$\hat{d}$	Kalman estimate of $d$ ; $\text{sgn}(\hat{d}) = -\text{sgn}(\tau_h)$ recovers the anatomical direction of patient torque
effort sign	<b>assist</b> ( $\sigma_{\text{eff}} > 0$ , torque aids the desired motion) vs. <b>resist/spasm</b> ( $\sigma_{\text{eff}} < 0$ , torque opposes it)
$\sigma_{\text{eff}} = \text{sgn}(\tau_h \dot{q}_d) = -\text{sgn}(\hat{d} \dot{q}_d)$	

### B. Patient Interaction Torque Model

The patient interaction torque  $\tau_h(t)$  has two physically distinct components:

$$\tau_h(t) = \underbrace{\tau_{\text{spasm}}(t)}_{\text{involuntary}} + \underbrace{\tau_{\text{vol}}(t)}_{\text{voluntary}} \quad (4)$$

*Spasm torque*  $\tau_{\text{spasm}}(t)$ : An impulsive or step-like contraction triggered by the stretch reflex when the robot stretches the muscle past a velocity threshold. In neurological patients (post-stroke, spinal cord injury), the stretch reflex is hyperactive—the reflex gain can be  $2\text{--}5\times$  the normal value—and the resulting torque typically opposes the robot’s trajectory. Simulation model: step onset  $\tau_{\text{spasm}} = \tau_0 = 15 \text{ Nm}$  at  $t = t_{\text{spasm}}$ , lasting 1.5 s (approximating a Modified Ashworth Scale Grade 2 spasm event).

*Voluntary torque*  $\tau_{\text{vol}}(t)$ : The net output of quadriceps, hamstrings, and gastrocnemius as the patient follows the prescribed trajectory. Positive  $\tau_{\text{vol}}$  (flexion-direction) indicates the patient is actively participating during a flexion command; negative  $\tau_{\text{vol}}$  (extension-direction) the converse. The lumped disturbance  $d(t) = -\tau_h(t)/I_{\text{eff}}$  can have either sign, which is the key rehabilitation-specific complexity: combining  $\hat{d}$  with the (known) desired-motion direction distinguishes AAN assist-reduction from spasm rejection (Section V-C).

*Sign conventions*. To avoid ambiguity between anatomical and motion-relative signs, all quantities follow Table I.

The anatomical sign of  $\hat{d}$  and the motion-relative effort sign  $\sigma_{\text{eff}}$  coincide only for a fixed desired-motion direction; the AAN logic (Section V-C) therefore uses  $\sigma_{\text{eff}}$ , which requires only  $\hat{d}$  and the reference velocity  $\dot{q}_d$  (no added sensor).

### C. Patient-Torque Estimation via Direct SEA Torque Sensing

We distinguish two quantities throughout: the spring deflection is a *direct measurement of the SEA output (transmitted) torque*  $\tau_r = k_s \delta$ , and the *patient torque*  $\tau_h$  is then **estimated** from it under the quasi-static balance (6). The latter is therefore a model-based estimate, not a direct measurement of patient torque; we use “direct SEA torque sensing used to estimate patient torque” in this precise sense. No dedicated 6-axis load cell is assumed. The spring deflection  $\delta = \theta_m/N - q$

is measured from the motor encoder and joint encoder. By Hooke’s law,

$$\tau_r = k_s \delta = k_s \left( \frac{\theta_m}{N} - q \right) \quad (5)$$

At quasi-static equilibrium ( $\ddot{q} \approx 0$ ,  $\dot{q} \approx 0$ ), Newton’s law at the knee gives

$$\tau_r \approx \tau_h(t) + \tau_g(q) \quad (6)$$

After gravity compensation (computed from known  $m_{\text{limb}}$ ,  $L_{\text{cm}}$ , and  $q$ ), the estimated patient interaction torque is

$$\hat{\tau}_h = k_s \delta - \tau_g(q) \approx \tau_h(t) \quad (7)$$

This is a *direct measurement of the SEA output torque used to estimate patient torque*—not a proxy via actuator current or fluid pressure—exact under the quasi-static assumption of (6) and subject to a residual from spring/limb acceleration at higher frequencies, with additional noise from encoder resolution and spring-stiffness uncertainty. The SEA measurement is strictly superior to hydraulic-pressure-based estimation: no fluid dynamics, no dead band from seal friction, and the spring deflection is available at the same rate as the encoder (typically 10–20 kHz), so the Kalman update period is set solely by the MPC rate (500 Hz).

In joint space, the disturbance state  $\hat{d} = -\hat{\tau}_h/I_{\text{eff}}$  (rad/s<sup>2</sup>); the negative sign follows from the error dynamics (9)–(10), in which—after the feedforward (8)—the patient torque enters  $\ddot{e}$  as  $-\tau_h/I_{\text{eff}}$ , so a trajectory-*opposing* spasm gives  $\hat{d} < 0$  (consistent with the Assist-as-Needed sign rule of Section V-C). The Kalman measurement matrix entry (Section IV-C) is therefore  $-I_{\text{eff}}$  (kg m<sup>2</sup>), mapping  $\hat{d}$  back to the measured torque  $[-I_{\text{eff}}][\hat{d}] = +\hat{\tau}_h$ , with units  $[\text{kg m}^2][\text{rad/s}^2] = \text{Nm}$  matching  $k_s \delta$  on the left.

#### D. Other Actuator Architectures

The Impedance MPC architecture is actuator-agnostic at the outer QP layer: the error dynamics (8)–(10) and the Kalman augmentation (11)–(12) depend only on  $I_{\text{eff}}$  and  $b_{\text{eff}}$ . Only the feedforward block and the Kalman measurement channel must be adapted. Table II summarises four alternatives for knee rehabilitation actuators.

*Hydraulic backdrivable actuators.* Compact hydraulic cylinders (as in [23]) achieve high torque density (>100 Nm/kg) and natural backdrivability, making them attractive for high-force rehabilitation. The feedforward (Section IV-A) is replaced by the hydraulic piston-space inversion of [23], and the Kalman channel uses slave-piston pressure  $A_2 P_2$  as in [23]. Bandwidth is typically 50–500 Hz, matching the SEA case.

*Quasi-direct-drive (QDD) motors.* Low gear ratio ( $N = 6$ –10) and large-diameter motors (T-Motor, Unitree actuators) provide high backdrivability with reflected inertia  $J_m N^2 \approx 0.01 \text{ kg m}^2$ , an  $8\times$  reduction over typical harmonic-drive gearboxes. The feedforward cancels the (small) reflected inertia and the Kalman channel uses motor current  $k_\tau i_m$  as the disturbance observation. QDD achieves the best transparency of any electrical actuator but is limited to  $\sim 60$  Nm peak torque for knee-scale devices.

TABLE II  
ACTUATOR ARCHITECTURE COMPARISON FOR KNEE REHABILITATION

Architecture	Peak torque	Back-driv.	Kalman channel	Control BW	Main limitation
SEA (this work)	60–80 Nm	Good	Spring defl. $k_s \delta$	50–500 Hz	BW limited by spring
Hydraulic	100+ Nm	Excellent	Slave press. $A_2 P_2$	50–500 Hz	Sealing; compress.
QDD motor	40–60 Nm	Excellent	Motor curr. $k_\tau i_m$	100–1000 Hz	Torque ceiling
Pneumatic PAM	40–70 Nm	Excellent	PAM gauge press.	5–10 Hz	Low BW; nonlinear
Cable-tendon	40–80 Nm	Good	Cable tension; curr.	100–1000 Hz	Routing; stretch

*Pneumatic artificial muscles (PAMs).* PAMs deliver high force-to-weight ratios and inherent compliance, making them mechanically safe for human contact. The feedforward inverts the McKibben pressure-force curve at each step. Bandwidth is limited by air compressibility to  $\sim 5$ –10 Hz, insufficient for the 500 Hz spasm-rejection rate required by this framework.

*Cable-tendon drives.* Lightweight Bowden-cable routing enables distal motor placement (ExoSuit, Harmony), reducing distal limb inertia. The joint-torque equation becomes  $\tau = r_f T_{\text{cable}} = r_f k_m i_m$  and the Kalman channel uses cable tension (load cell) or motor current. Peak torque is typically 40–80 Nm, sufficient for knee rehabilitation.

## IV. IMPEDANCE MPC DESIGN

### A. Architecture Overview

The controller has two layers.

**Layer 1 — Feedforward.** An algebraic term cancels the known SEA plant dynamics (effective inertia, damping, gravity), leaving a scalar double integrator as the residual plant:

$$\tau_{\text{ff}} = I_{\text{eff}} \ddot{q}_d + b_{\text{eff}} \dot{q} + \tau_g(q) \quad (8)$$

The inertia term uses the reference acceleration  $\ddot{q}_d$ ; the damping term uses the *actual* joint velocity  $\dot{q}$ , so  $b_{\text{eff}} \dot{q}$  cancels the physical damping exactly and leaves  $A_c$  a constant double integrator. In hardware  $\dot{q}$  is low-pass filtered (e.g., 250 Hz, <1 ms lag) against encoder-quantization noise; the small filter lag is *not* added to the prediction model but lumped into  $d(t)$  and absorbed by the Kalman state, so the model stays constant- $A_d$  and offset-free—the disturbance-absorption device established in the base framework [33]. The gravity term  $\tau_g(q)$  needs only three offline-identified parameters ( $I_{\text{eff}}$ ,  $b_{\text{eff}}$ ,  $m_{\text{limb}} L_{\text{cm}}$ ) from perturbation tests and anthropometric tables [16], keeping the approach demonstration-free.

**Layer 2 — Impedance MPC.** A receding-horizon QP computes a corrective torque  $\tau_{\text{mpc}}$  on the residual double integrator to minimize tracking error while enforcing hard constraints on ROM, actuator torque, and joint velocity over a prediction horizon of  $N$  steps.

## B. Scalar Error Dynamics

Define  $e = q_d - q$  and decompose  $\tau = \tau_{ff} + \tau_{mpc}$ . After applying (8) and substituting into (3), the residual error dynamics are

$$\ddot{e} = -\Gamma_e \tau_{mpc} + d(t) \quad (9)$$

where  $d(t) = -\tau_h(t)/I_{\text{eff}}$  aggregates all unmodeled terms (patient interaction torque, gravity residual, Coriolis) normalized to acceleration units—the negative sign because, after the feedforward (8), the patient torque enters the error as  $\ddot{e} = -\Gamma_e \tau_{mpc} - \tau_h/I_{\text{eff}}$ —and  $\Gamma_e = 1/I_{\text{eff}} = 2.22 \text{ rad s}^{-2} \text{ Nm}^{-1}$ . The state  $x_e = [e, \dot{e}]^\top \in \mathbb{R}^2$  satisfies

$$\dot{x}_e = \underbrace{\begin{bmatrix} 0 & 1 \\ 0 & 0 \end{bmatrix}}_{A_c} x_e + \underbrace{\begin{bmatrix} 0 \\ -\Gamma_e \end{bmatrix}}_{B_c} \tau_{mpc} + \underbrace{\begin{bmatrix} 0 \\ 1 \end{bmatrix}}_{G_c} d(t) \quad (10)$$

The disturbance enters through  $G_c = [0, 1]^\top$ , distinct from the control matrix  $B_c = [0, -\Gamma_e]^\top$  ( $G_c$  carries  $d$  directly;  $B_c$  scales  $\tau_{mpc}$  by  $-\Gamma_e$ ). As in the base framework [33],  $A_c$  is nilpotent ( $A_c^2 = 0$ ), so the discrete  $A_d$  is exact and configuration-independent with closed-form ZOH matrices:

$$A_d = \begin{bmatrix} 1 & \Delta t \\ 0 & 1 \end{bmatrix}, \quad B_d = \begin{bmatrix} -\frac{\Delta t^2}{2} \Gamma_e \\ -\Delta t \Gamma_e \end{bmatrix}, \quad G_d = \begin{bmatrix} +\frac{\Delta t^2}{2} \\ +\Delta t \end{bmatrix} \quad (11)$$

( $G_d = -B_d/\Gamma_e$ : positive and not  $\Gamma_e$ -scaled, since the disturbance enters the error directly.) This constant- $A_d$  reduction—and the resulting offline precomputation of  $\Phi$ ,  $\Gamma$ ,  $H = \Gamma^\top \bar{Q} \Gamma + \bar{R}$  and  $H^{-1}$ —is the core result of [33], here specialized to the scalar knee. The online unconstrained step is the single multiply  $U^* = -H^{-1}f$  (measured at  $\approx 3 \mu\text{s}$ ; Table III); when the constraints (15) bind, OSQP reuses the cached factorization (tens of  $\mu\text{s}$ ; Table III). In Sections VI–VII the ROM/velocity limits stay inactive, so the closed-form step applies with actuator saturation by clipping. The benchmarks fix  $N = 20$  across all seven controllers so the no-Kalman ablations (D4/D6) are compared at a common horizon; the *deployed* Kalman controller is horizon-insensitive—because the integrating disturbance state, not look-ahead, sets its accuracy—so it runs at  $N = 10$  (halving the Hessian and the online multiply) with no meaningful change (D7 steady-state  $0.09 \rightarrow 0.13 \text{ mrad}$ , both  $\ll$  the  $87 \text{ mrad}$  criterion). **To be unambiguous: all benchmark results in Tables V and VII use  $N = 20$ ;  $N = 10$  appears only as a deployment-side optimization (Fig. 2 and the Section VIII projection), never in the headline benchmark tables.**

## C. Disturbance Augmentation for Offset-Free Tracking

Following the base framework [33] and offset-free MPC theory [20], the error state is augmented with an integrating disturbance state  $\hat{d} \in \mathbb{R}$  (rad/s<sup>2</sup>, the normalized patient torque) estimated by a steady-state Kalman filter; under mild observability it tracks any constant or slowly-varying patient torque exactly, eliminating steady-state error without the integral windup that afflicts sequential spasms [24], [25]:

$$\begin{bmatrix} x_e(k+1) \\ \hat{d}(k+1) \end{bmatrix} = \underbrace{\begin{bmatrix} A_d & G_d \\ 0 & 1 \end{bmatrix}}_A \begin{bmatrix} x_e(k) \\ \hat{d}(k) \end{bmatrix} + \begin{bmatrix} B_d \\ 0 \end{bmatrix} \tau_{mpc}(k) \quad (12)$$

where the disturbance enters through the positive column  $G_d$ , distinct from the control column  $B_d$  (cf. (11)). A steady-state Kalman filter estimates  $\hat{d}(k)$  from three measurements:

$$y_k = \begin{bmatrix} 1 & 0 & 0 \\ 0 & 1 & 0 \\ 0 & 0 & -I_{\text{eff}} \end{bmatrix} \begin{bmatrix} e \\ \dot{e} \\ \hat{d} \end{bmatrix}_k + v_k \quad (13)$$

The third measurement  $y_3 = k_s \delta - \tau_g(q) \approx \hat{\tau}_h = -I_{\text{eff}} \hat{d}$  follows from (7): the gravity-compensated spring deflection directly estimates the patient interaction torque, which maps to the disturbance state via  $\hat{d} = -\hat{\tau}_h/I_{\text{eff}}$  (the sign matching the error dynamics (9)–(10), where the patient torque enters  $\ddot{e}$  negatively). The  $C$ -matrix entry  $-I_{\text{eff}}$  (kg m<sup>2</sup>) converts  $\hat{d}$  (rad/s<sup>2</sup>) back to the measured torque:  $[-I_{\text{eff}}][\hat{d}] = +\hat{\tau}_h$ , with  $[\text{kg m}^2][\text{rad/s}^2] = \text{Nm}$  matching  $k_s \delta$  on the left. This measurement channel provides a *direct SEA-based*, noise-optimal torque estimate, reducing estimator lag from 5–10 QP periods (encoder-only Kalman) to a few periods—the steady-state Kalman gain on this channel is  $\approx -1/I_{\text{eff}}$ , i.e. it inverts the direct torque measurement rather than integrating a position residual—a structural advantage over hydraulic-pressure-based estimation [23], which relies on a proxy  $A_2 P_2$  rather than a direct spring-force measurement.

*Remark 1 (Sensor requirements).* Three hardware configurations are supported:

Configuration	Convergence	Practical outcome
No Kalman (D4/D6)	—	SS error well below classical impedance at high $Q/R$ ( $\approx 25 \text{ mrad}$ vs. 515); depends on $Q/R$
Encoder-only Kalman	5–10 QP periods	$\sim 10$ – $20 \text{ ms}$ at 500 Hz; offset-free at any $Q/R$
Full Kalman with $k_s \delta$ (D5/D7)	$\sim 1$ – $2$ QP periods	$\sim 2$ – $4 \text{ ms}$ at 500 Hz; offset-free + fastest transient

The SEA spring encoder is standard hardware in any SEA-equipped exoskeleton; the Kalman channel is therefore effectively free on modern platforms.

The integrating disturbance state provides a *nominal* offset-free guarantee [20]—exact for a **constant or slowly-varying** disturbance, under **observability** of the augmented system (12)–(13), convergence of the steady-state Kalman filter, and **recursive feasibility** of the QP (Section IV-F); it is not claimed for fast-varying disturbances, model error, or infeasible horizons. Under these conditions, once  $\hat{d}$  converges to  $d = -\tau_h/I_{\text{eff}}$ , the steady-state prediction error is driven to zero. This is the dominant contributor to steady-state accuracy under sustained spasm. Without the estimator the MPC is a predictive realization of a classical impedance, so its steady-state error is set by the realized stiffness and the sampling interval ( $8.3 \text{ mrad}$  for the no-Kalman D6, Table V); the Kalman augmentation removes this offset, reducing the steady-state error to  $0.1 \text{ mrad}$  (D7)—an essentially complete elimination of the systematic offset. Crucially, because the *direct*  $k_s \delta$  spring-deflection channel is inverted by the Kalman gain ( $\approx -1/I_{\text{eff}}$ ) rather than reconstructed from a position residual,  $\hat{d}$  converges within a few QP periods, so the offset is cancelled near-immediately at contact onset. We quantify this three ways: (i)

the steady-state observer-error eigenvalue associated with the  $\hat{d}$  channel is  $|\lambda_d| \approx 0.09$  at 500 Hz (near-deadbeat), while the slower  $|\lambda| \approx 0.78\text{--}0.90$  modes belong to the position/velocity estimates, not the disturbance; (ii) in a step-disturbance test the estimate  $\hat{d}$  reaches within 5% of the step in a single sample at 500 Hz (noise-limited to  $\sim 8$  samples at 100 Hz); and (iii) operationally, the contact-window peak collapses to 0.2 mrad (D7) from 8.3 mrad (D6)—the offset-free benefit is realized in the transient as well as at steady state, and the 0.2 mrad onset peak is the measured end-to-end evidence. Unlike PI impedance, the observer gain is structured (Kalman-optimal), preventing windup across sequential spasm events [24], [25].

*Remark 2 (Bidirectional disturbance).* Unlike grasping (where object contact always opposes the finger), the patient torque—and hence  $\hat{d}$ —can be positive or negative. The Kalman state  $\hat{d}$  tracks the disturbance  $d = -\tau_h/I_{\text{eff}}$  (Table I): its sign recovers the *anatomical* direction of patient torque, while *assist vs. resist* is the **motion-relative** quantity  $\sigma_{\text{eff}} = \text{sgn}(\tau_h \dot{q}_d) = -\text{sgn}(\hat{d} \dot{q}_d)$ , which combines  $\hat{d}$  with the known reference velocity  $\dot{q}_d$ . The AAN extension (Section V-C) uses  $\sigma_{\text{eff}}$  together with  $|\hat{d}|$  to trigger cost-matrix scheduling that reduces robot stiffness when the patient actively contributes—without requiring a separate intent-detection subsystem.

#### D. Receding-Horizon QP

**Prediction stack.** Applying (11) recursively and stacking the  $N$  predicted error states into  $Y = [x_e^\top(1), \dots, x_e^\top(N)]^\top \in \mathbb{R}^{2N}$  gives  $Y = \Phi x_0 + \Gamma U$ , where  $x_0 = x_e(t)$  is the current error state,  $U = [\tau_{\text{mpc}}(0), \dots, \tau_{\text{mpc}}(N-1)]^\top \in \mathbb{R}^N$ , and

$$\Phi = \begin{bmatrix} A_d \\ A_d^2 \\ \vdots \\ A_d^N \end{bmatrix} \in \mathbb{R}^{2N \times 2}, \quad \Gamma = \begin{bmatrix} B_d & & & \\ A_d B_d & B_d & & \\ \vdots & \ddots & & \\ A_d^{N-1} B_d & \cdots & B_d & \end{bmatrix} \in \mathbb{R}^{2N \times N}$$

Because  $A_d$  is constant, both  $\Phi$  and  $\Gamma$  are precomputed offline. When the Kalman disturbance estimate  $\hat{d}$  is active, the full prediction reads  $Y = \Phi x_0 + \Gamma U + \Delta(\hat{d})$  with

$$\Delta_k(\hat{d}) = \left( \sum_{i=0}^{k-1} A_d^i \right) G_d \hat{d}, \quad k = 1, \dots, N, \quad G_d = \begin{bmatrix} +\frac{\Delta t^2}{2} \\ +\Delta t \end{bmatrix}.$$

$G_d = [+ \Delta t^2/2, + \Delta t]^\top$  is positive (disturbance *increases* error); this is consistent with (9)–(11) and differs in sign from  $B_d$  (which is negative because control *decreases* error). Substituting into the horizon cost  $\sum_{k=1}^N [x_e(k)^\top Q x_e(k) + R_u \tau_{\text{mpc}}(k-1)^2]$  and completing the square yields the condensed cost matrices

$$H = \Gamma^\top \bar{Q} \Gamma + \bar{R}, \quad f = \Gamma^\top \bar{Q} (\Phi x_0 + \Delta(\hat{d})) \quad (14a)$$

where  $\bar{Q} = \text{blkdiag}(Q, \dots, Q, Q_f) \in \mathbb{R}^{2N \times 2N}$  and  $\bar{R} = R_u I_N$ . Both  $H$  and  $H^{-1}$  are precomputed offline. At each MPC step, the condensed QP solved over  $U$  is

$$\min_U \frac{1}{2} U^\top H U + f^\top U \quad (14)$$

TABLE III  
MEASURED ONLINE PER-STEP SOLVE TIME

Online step	$N$	Mean	p99	Budget
Closed-form $-H^{-1}f$ (inactive)	10	2.9 $\mu\text{s}$	3.2 $\mu\text{s}$	2000 $\mu\text{s}$
Closed-form $-H^{-1}f$ (active)	20	3.0 $\mu\text{s}$	3.4 $\mu\text{s}$	2000 $\mu\text{s}$
OSQP warm-start (inactive)	10	18 $\mu\text{s}$	25 $\mu\text{s}$	2000 $\mu\text{s}$
OSQP warm-start (active)	20	27 $\mu\text{s}$	37 $\mu\text{s}$	2000 $\mu\text{s}$

Apple M1 Max, single thread, Python 3 / NumPy 2.4 / SciPy 1.17 / OSQP 1.1;  $2 \times 10^5$  trials closed-form,  $2 \times 10^4$  OSQP.

subject to

$$\begin{aligned} \tau_{\text{ff}}(k) + \tau_{\text{mpc}}(k) &\in [-\tau_{\text{max}}, \tau_{\text{max}}] && \text{(torque: ISO 13482)} \\ q_d(k) - e(k) &\in [q_{\text{min}}, q_{\text{max}}] && \text{(ROM constraint)} \\ |\dot{q}_d(k) - \dot{e}(k)| &\leq \omega_{\text{max}} && \text{(velocity limit)} \\ |\Delta \tau_{\text{mpc}}(k)| &\leq \Delta \tau_{\text{max}} && \text{(jerk/rate limit)} \end{aligned} \quad (15)$$

with  $\tau_{\text{max}} = 60 \text{ Nm}$  (ISO 13482 [10]),  $q_{\text{min}} = 0$ ,  $q_{\text{max}} = 2.094 \text{ rad}$  ( $120^\circ$ ),  $\omega_{\text{max}} = 2.0 \text{ rad/s}$ . The decision variable  $U$  is in torque units (Nm), so  $\tau_{\text{max}}$  applies directly to  $\tau_{\text{ff}} + \tau_{\text{mpc}}$ . Only  $\tau_{\text{mpc}}(0)$  is applied (receding principle); the QP is solved with OSQP [21], reusing the cached KKT factorization.

**Per-step runtime.** Table III reports the measured online cost. When the ROM/velocity constraints are inactive (Sections VI–VII), the step is the closed-form multiply  $U^* = -H^{-1}f$  with  $f$  from (14a)—a few microseconds; when they bind, the warm-started OSQP solve reusing the cached factorization stays in the tens of microseconds. Both are two orders of magnitude inside the 2000  $\mu\text{s}$  budget of the 500 Hz loop, so the 500 Hz claim has substantial margin even on a general-purpose CPU.

**Reproducibility.** The timed operation is the full online step: forming  $f = \Gamma^\top \bar{Q} (\Phi x_0 + \Delta(\hat{d}))$  and the multiply  $U^* = -H^{-1}f$  (closed-form rows), or one warm-started OSQP update+solve reusing the cached factorization (OSQP rows). Operand dimensions:  $H, H^{-1} \in \mathbb{R}^{N \times N}$ ,  $\Phi \in \mathbb{R}^{2N \times 2}$ ,  $\Gamma \in \mathbb{R}^{2N \times N}$ , all loop-resident float64 NumPy arrays (vendor BLAS/Accelerate). Timing is steady-state, cache-warm (the constant matrices are precomputed once offline and the first calls are amortized over the  $2 \times 10^5/2 \times 10^4$  trials); mean and p99 are reported, the sub-millisecond outliers in the raw trace being OS scheduling/GC artifacts, not algorithmic cost. These are desktop (non-real-time OS) figures in an interpreted-Python harness—an embedded C/real-time target would only tighten them and remove the jitter tail; worst-case timing on the intended embedded controller is left to the hardware study (Section IX).

#### E. Disturbance Prediction Over the Horizon

The QP of Section IV-D extrapolates the disturbance across the horizon by the integrating Kalman’s random-walk prior,  $\hat{d}(k+j|k) = \hat{d}(k)$ . Over the knee’s short horizon ( $N\Delta t = 40 \text{ ms}$  at 500 Hz) the patient torque changes negligibly, so this constant model is accurate and is used throughout Sections VI–VII. A sign-aware, exponentially-decaying extrapolation (with

a per-event Kalman process-noise schedule) can in principle improve the spasm-release phase on low-bandwidth actuators (Table II) or under reduced-gain tuning, where the disturbance feedforward—rather than position feedback—dominates the command; it admits a closed-form horizon term that leaves the Hessian (and hence the offline  $H^{-1}$ ) unchanged and reduces to the constant model as the decay rate vanishes, preserving the offset-free guarantee. In the high-authority knee regime, however, feedback dominates and the two models give numerically identical tracking (D7 unchanged); quantifying the benefit on slower platforms is left to future work.

### F. Equivalence to Classical Impedance

In the unconstrained, disturbance-free limit with  $Q = \text{diag}(K_d, D_d)$  and  $R_u \rightarrow 0$ , the infinite-horizon MPC recovers the classical joint-impedance law [33]:

$$\tau^{\text{cmd}} = I_{\text{eff}} \ddot{q}_d + b_{\text{eff}} \dot{q} + \tau_g(q) + K_d e + D_d \dot{e} \quad (16)$$

giving the design rule  $Q_{\text{pos}} = K_d$ ,  $Q_{\text{vel}} = D_d$ ; the MPC strictly extends this whenever constraints or patient disturbances are active. The terminal weight  $Q_f = 5Q$  used in the benchmarks is a performance heuristic; a formal unconstrained-stability certificate sets  $Q_f$  to the DARE solution, with constraint satisfaction following from recursive feasibility under (17), as established in [33], [6].

## V. REHABILITATION-SPECIFIC EXTENSIONS

### A. ROM Constraint Linearization in QP

The state constraint  $q_{\min} \leq q(k) \leq q_{\max}$  is expressed in terms of the error state via  $q(k) = q_d(k) - e(k)$ :

$$q_d(k) - e(k) \geq q_{\min} \Rightarrow e(k) \leq q_d(k) - q_{\min} \quad (17a)$$

$$q_d(k) - e(k) \leq q_{\max} \Rightarrow e(k) \geq q_d(k) - q_{\max} \quad (17b)$$

Since  $e(k)$  is linear in  $U$  via the prediction stack, constraints (17) add two rows per prediction step to the QP inequality set—a total of  $2N$  additional rows for an  $N$ -step horizon. Enforcing (17) as hard QP inequalities yields ROM compliance at every predicted step—not only at the current time—provided recursive feasibility is maintained (an assumption discussed for the terminal weight in Section IV-F). This is the critical distinction from post-hoc saturation: saturation changes the applied torque after the QP solution is computed, violating the optimality certificate and potentially causing integrator windup in the error state. The velocity constraint  $|\dot{q}(k)| \leq \omega_{\max}$  is handled identically via  $\dot{q}(k) = \dot{q}_d(k) - \dot{e}(k)$ .

**Clinical significance.** For a post-ACL patient with surgeon-prescribed ROM limit of  $100^\circ = 1.745 \text{ rad}$ , the QP constraint  $q_{\max} = 1.745 \text{ rad}$  keeps every predicted step within this limit while the QP is feasible—even during the high-acceleration onset of a spasm event. This provides a stronger safety guarantee than hardware end-stops alone, which engage only at the constraint boundary rather than predictively.

### B. Energy-Bounded Interaction via an Energy Tank

To encourage energy-bounded interaction with the patient limb, the QP can be augmented with an energy-tank constraint inspired by passivity-based MPC [7]:

$$T_{k+1} = T_k + \tau_{h,k} \dot{q}_k \Delta t - \tau_{\text{mpc},k} \dot{q}_k \Delta t, \quad T_k \geq 0 \quad \forall k \quad (18)$$

Using  $\hat{\tau}_h = k_s \delta$  as the estimated patient torque in the energy balance, constraint (18) bounds the energy the controller can inject into the human limb. This is an energy-budget constraint, not a formal passivity proof: with an exact torque estimate and the tank dynamics (18) it enforces non-negative tank energy at every predicted step, but a rigorous discrete-time passivity certificate (storage function, and preservation under the other active constraints) is left to future work. It adapts the energy-tank idea of [7] to the receding-horizon rehabilitation setting.

**Rehabilitation interpretation.** When  $T \rightarrow 0$ , the robot switches to energy-neutral mode: it can only dissipate energy (damp oscillations), not inject it. This is precisely the correct behavior during a spasm event—damp the reflex contraction rather than fight it—and provides an automatic, physics-grounded safety mechanism that supplements the explicit torque constraint (15).

### C. Sensorless Assist-as-Needed via Disturbance Sign

The motion-relative effort sign  $\sigma_{\text{eff}}$  (Table I) encodes whether the patient's torque aids or opposes the desired motion:

$$\sigma_{\text{eff}}(t) = \text{sgn}(\tau_h \dot{q}_d) = -\text{sgn}(\hat{d} \dot{q}_d) = \begin{cases} + & \text{torque aids motion} \\ - & \text{torque opposes (spasm)} \end{cases} \quad (19)$$

This requires only the estimate  $\hat{d}$  and the known reference velocity  $\dot{q}_d$ —no added sensor. When  $\sigma_{\text{eff}} > 0$  and  $|\hat{d}| > d_{\text{threshold}}$  (patient actively assists), the QP cost matrix is scheduled to reduce virtual stiffness:

$$K_d(t) = \max(K_{\min}, K_{\text{nominal}} - \alpha_{\text{AAN}} |\hat{d}|) \quad (20)$$

where  $K_{\min}$  is the minimum safe stiffness (prevents ROM violation under maximum expected spasm) and  $\alpha_{\text{AAN}}$  is the AAN gain (Nm/rad per rad/s<sup>2</sup>). The robot steps back proportionally to the patient's detected effort—implementing true Assist-as-Needed at the same update rate (500 Hz) as the trajectory tracking loop, without requiring sEMG electrodes, their electrode-placement variability, or their session-by-session calibration required by EMG-driven joint-torque estimation. During a pure isometric hold ( $\dot{q}_d = 0$ ) there is no motion to assist, so  $\sigma_{\text{eff}}$  is inactive and the controller defaults to spasm rejection.

When  $\sigma_{\text{eff}} < 0$  with  $|\hat{d}| > d_{\text{threshold}}$  (spasm or resistance detected), the cost matrix reverts to  $K_{\text{nominal}}$  to maintain the prescribed trajectory within the hard QP torque constraint (15). Because the torque constraint is hard rather than soft, the robot neither escalates beyond  $\tau_{\text{max}}$  to fight a spasm (force duel) nor abandons the trajectory entirely (admittance failure). This is the key distinction from both stiff position control (cannot yield safely) and admittance control (cannot reject safely).

**Spasm detection latency.** At 500 Hz, the Kalman filter detects  $|\hat{d}| > d_{\text{threshold}}$  within 2–4 update steps (4–8 ms) of a step-change in patient torque. This is well within the tens-of-milliseconds reflex window over which spastic forces build (cf. the stretch-reflex latencies discussed in [1]). At 100 Hz, detection latency is 50–100 ms—comparable to or beyond the interval over which a stretch reflex builds. In our simulations, 500 Hz is therefore *preferred* for rapid spasm detection and for minimizing onset transients (Tables V, VII); we do not claim it as an experimentally-established physiological threshold, which would require human spasm data and is left to the clinical study (Section IX).

#### D. Multi-Joint Extension for Bilateral Rehabilitation

For bilateral knee rehabilitation (or hip-knee coupled systems), the Impedance MPC architecture decouples naturally: each joint runs an independent 1D QP in joint space. Sagittal-plane coupling between hip and knee (arising from hamstring biarticularity and common attachment) enters as a higher-level coordination constraint: the net joint torque pattern must produce a desired limb endpoint trajectory, which yields a joint QP with  $n$  decision vectors—solvable in  $<1$  ms for  $n = 4$  joints (bilateral hip+knee) at  $N = 20$  on modern embedded hardware.

### VI. SIMULATION STUDY: SINUSOIDAL TRACKING UNDER PATIENT SPASM

#### A. Scenario

Seven controllers are evaluated on a sinusoidal tracking task under step patient spasm. The reference trajectory is

$$q_d(t) = \bar{q} + r(t) A_q \sin(\omega_q t), \quad \bar{q} = 1.047 \text{ rad } (60^\circ), \quad A_q = 0.524 \text{ rad} \quad (21)$$

with  $A_q = 0.524 \text{ rad } (30^\circ)$ ,  $\omega_q = \pi/2 \text{ rad/s}$ , and  $r(t) = \min(1, t/1.0)$  for a smooth start. A step patient spasm torque  $\tau_h = 15 \text{ Nm}$  is applied at the knee joint from  $t = 1.5$  to  $t = 3.0 \text{ s}$  in each 4 s cycle (opposing the motion), then released. Four cycles (16 s total) are simulated. *Gravity note:* the feedforward (8) cancels gravity exactly via  $\tau_g(q)$ ; the simulation therefore models the gravity-compensated residual plant  $I_{\text{eff}}\ddot{q} + b_{\text{eff}}\dot{q} = \tau_{\text{mpc}} + \tau_h$ . This is representative of the seated rehabilitation posture where gravity loading on the shank is largely balanced by the robot's gravity-compensation torque. Plant parameters:  $I_{\text{eff}} = 0.45 \text{ kg m}^2$ ,  $b_{\text{eff}} = 0.50 \text{ Nm s/rad}$ ,  $\Gamma_e = 1/I_{\text{eff}} = 2.22 \text{ rad s}^{-2} \text{ Nm}^{-1}$ .

The normalized disturbance is  $d = -\tau_h/I_{\text{eff}} = -33.3 \text{ rad/s}^2$  (sign per (9)–(13); magnitude  $|d| = 15/0.45 = 33.3 \text{ rad/s}^2$ ). The moderate magnitude of  $d$  relative to the correction authority  $\tau_{\text{max}}/I_{\text{eff}} = 133 \text{ rad/s}^2$  means the MPC has ample headroom to compensate—yet with a fixed-gain controller (D1) the steady-state error still reaches 500 mrad, because no fixed-gain controller can simultaneously track and reject a constant unknown offset.

#### B. Controllers

Table IV describes the seven controllers evaluated (D1–D7). D1–D3 are classical baselines; D4–D7 are Impedance MPC

TABLE IV  
CONTROLLERS EVALUATED IN SIMULATION

ID	Controller	Rate	Disturbance Est.
D1	Classical ( $K_d = 30$ )	Impedance 1 kHz	None
D2	Admittance ( $K_a = 10$ )	1 kHz	None
D3	PI Impedance ( $K_{\text{int}} = 8$ )	1 kHz	Integral
D4	Impedance MPC (no Kalman)	QP 100 Hz	None
D5	Impedance MPC + Kalman	QP 100 Hz	Kalman $\hat{d}$
D6	Impedance MPC 500 Hz	QP 500 Hz	None
D7	Impedance MPC + Kalman 500 Hz	QP 500 Hz	Kalman $\hat{d}$

TABLE V  
SINUSOIDAL TRACKING RESULTS ( $\tau_h = 15 \text{ Nm}$ , 16 s / 4 CYCLES) — SIMULATION

Controller	RMS tot. (mrad)	RMS cnt. (mrad)	Peak (mrad)	SS (mrad)
D1 — Impedance	322	504	713	515
D2 — Admittance <sup>†</sup>	831	1226	1570 <sup>†</sup>	1551
D3 — PI Impedance	271	373	697	319
D4 — MPC 100 Hz (no K.)	15	24	25	25
D5 — MPC + Kalman 100 Hz	<b>0.5</b>	<b>0.6</b>	<b>3.4</b>	<b>0.1</b>
D6 — MPC 500 Hz	4.8	7.7	8.3	8.3
D7 — MPC + Kalman 500 Hz	<b>0.1</b>	<b>0.1</b>	<b>0.2</b>	<b>0.1</b>

<sup>†</sup>ROM safety stop engaged; full deflection would exceed 120° ROM limit without constraint enforcement.

variants with different update rates and disturbance estimation. D4/D5 use  $\Delta t_{\text{MPC}} = 10 \text{ ms}$  (100 Hz, 200 ms horizon), D6/D7 use  $\Delta t_{\text{MPC}} = 2 \text{ ms}$  (500 Hz, 40 ms horizon). D5/D7 include the Kalman augmentation; D4/D6 do not. All MPC variants use  $N = 20$ ,  $Q_{\text{pos}} = 2 \times 10^4$ ,  $Q_{\text{vel}} = 100$ ,  $Q_{f,\text{scale}} = 5$ ,  $R_u = 10^{-5}$ ,  $\tau_{\text{max}} = 60 \text{ Nm}$ .

#### C. Results

Table V (visualized in Fig. 1) reports all four tracking metrics. *RMS total:* root-mean-square error over the full 16 s. *RMS contact:* RMS restricted to spasm-on windows  $t_{\text{cyc}} \in [1.5, 3.0] \text{ s}$ . *Peak deflection:* maximum  $|e(t)|$  during spasm-on windows. *Steady-state (SS) error:* mean  $|e(t)|$  over the last 0.2 s of each spasm window.

**Reading the table — estimator vs. rate.** Note that D5 (100 Hz + **Kalman**) outperforms D6 (500 Hz, **no Kalman**): 0.5 vs. 4.8 mrad RMS, 0.1 vs. 8.3 mrad SS. This demonstrates that the **disturbance estimator contributes more to steady-state accuracy than the sampling rate**—adding the Kalman at 100 Hz beats quintupling the rate without it. D6 is included specifically to isolate the rate effect in the *absence of disturbance estimation* (compare D4→D6); the estimator

effect is isolated by D4→D5 and D6→D7. The two factors are quantified separately in Section VI-D.

*Note:* Unlike the hydraulic hand case (Cao et al. [23]), D4 does not degrade vs. D1 here. The knee’s large effective inertia ( $I_{\text{eff}} = 0.45 \text{ kg m}^2$ ) gives a small normalized disturbance ( $|d| = 33.3 \text{ rad/s}^2$ ) relative to the MPC’s correction authority ( $\tau_{\text{max}}/I_{\text{eff}} = 133 \text{ rad/s}^2$ ), and the  $4\times$  torque headroom prevents the saturation-induced oscillations that made D4 fail in the hand case. The Kalman (D5/D7) then eliminates the residual steady-state offset that position feedback alone leaves—cutting SS from 25 → 0.1 mrad at 100 Hz (D4→D5) and 8.3 → 0.1 mrad at 500 Hz (D6→D7)—and additionally provides (i) a *nominal* offset-free certificate (under the Section IV-C assumptions) independent of  $Q/R$  tuning (decisive when  $R_u$  is raised for safety, lowering the realized stiffness so feedback alone no longer cancels the offset), (ii) sign-based AAN (Section V-C), and (iii) the fastest transient via the direct  $k_s\delta$  channel (D7 peak 0.2 mrad).

#### D. Analysis

**D1 matches theory exactly.** Classical impedance reaches SS error = 515 mrad, matching  $e_\infty = \tau_h/K_d = 15/30 = 500 \text{ mrad}$  (simulation residual 3%). Peak = 713 mrad > SS because the spasm fires during sinusoidal motion, adding trajectory-tracking error to the SS offset before the disturbance settles. This confirms simulation fidelity and validates the plant identification.

**Admittance yields by design—with ROM safety consequence.** D2 interprets the patient spasm as therapeutic guidance intent and drives the knee toward the spasm direction. SS error = 1551 mrad  $\approx \tau_h/K_a = 15/10 = 1500 \text{ mrad}$ . The ROM safety stop engages at  $120^\circ$  on each flexion half-cycle, demonstrating that admittance control is unsafe during passive-stretching phases without additional ROM constraint enforcement.

**Integral action partially cancels, but slowly.** D3 reduces SS error from 515 to 319 mrad. The 1.5 s spasm window is insufficient for full integral convergence at  $K_{\text{int}} = 8 \text{ Nm/(rad s)}$  under the anti-windup limit, and cross-contamination between consecutive spasm events corrupts subsequent approach phases [24], [25].

**MPC outperforms classical impedance even without Kalman.** This result is structurally different from the hydraulic hand case [23]. D4 (MPC at 100 Hz, no Kalman) achieves SS = 25 mrad—well below D1’s 515 mrad—rather than degrading as in [23]. The root cause: the knee’s  $I_{\text{eff}} = 0.45 \text{ kg m}^2$  gives a normalized disturbance  $|d| = 33.3 \text{ rad/s}^2$  and a torque correction headroom  $\tau_{\text{max}}/I_{\text{eff}} = 133 \text{ rad/s}^2$  (4:1 ratio). The MPC with  $Q/R = 2 \times 10^9$  applies essentially the optimal  $-\tau_{\text{patient}}$  correction through position-error feedback, whereas in [23] the smaller hand inertia and near-saturated actuator caused limit-cycle oscillations. Physically: **the knee is a less demanding disturbance-rejection problem because the patient’s spasm is small relative to the available corrective authority.**

**Kalman eliminates the steady-state offset.** Adding the disturbance-state augmentation drives the steady-state error to

the offset-free floor at both rates: D5 (100 Hz + Kalman) cuts SS from 25 mrad (D4) to 0.1 mrad, and D7 (500 Hz + Kalman) from 8.3 mrad (D6) to 0.1 mrad. This is the central role of the integrating disturbance state: position feedback alone leaves a sampling-dependent residual (25 mrad at 100 Hz, 8.3 mrad at 500 Hz), whereas the propagated  $\hat{d}$  cancels it. The augmentation contributes three further benefits in the knee context: (i) the offset-free property is a *formal* guarantee independent of  $Q/R$  tuning—decisive when  $R_u$  must be increased for safety certification (lowering realized stiffness, so the no-Kalman residual grows while the Kalman variant stays at 0.1 mrad); (ii) the sign of  $\hat{d}$  enables the AAN mechanism (Section V-C) without EMG; and (iii) the direct  $k_s\delta$  channel gives the fastest onset transient (D7 peak 0.2 mrad).

A fourth, latency-related consideration provides an *engineering rationale* (not a physiological conclusion) for the 500 Hz rate. At 500 Hz the augmented filter identifies a step change in  $\hat{d}$  and reschedules the cost matrix within 4–8 ms (2–4 QP steps, Section V-C); for reference, spinal stretch-reflex escalation occurs on a  $\sim 40 \text{ ms}$  scale [1], so at 500 Hz the controller can begin adapting its compliance within that window rather than after it, as the 100 Hz variant (50–100 ms detection latency) and every classical baseline would. We present this as the engineering motivation for the bounded 0.2 mrad onset peak of D7 (and the AAN response) versus the 713 mrad peak of classical impedance (D1) *in simulation*; whether this faster adaptation yields a clinically meaningful benefit over 100 Hz is not established here and would require human spasm data (Section IX).

**Steady-state error is governed by the Kalman; the transient peak by the rate.** The two contributions are orthogonal. (i) *Estimation drives steady state:* adding the Kalman cuts the steady-state error from 25 mrad to 0.1 mrad at 100 Hz (D4→D5) and from 8.3 mrad to 0.1 mrad at 500 Hz (D6→D7)—offset-free at either rate. (ii) *Rate drives the transient.* Without the estimator, the no-Kalman steady-state error itself falls from 25 mrad (D4, 100 Hz) to 8.3 mrad (D6, 500 Hz) because the realized stiffness rises with rate and the ZOH lag shrinks—the disturbance accumulates  $|d| \cdot \Delta t_{\text{MPC}}^2/2 = 33.3 \times (0.01)^2/2 = 1.7 \text{ mrad}$  per 100 Hz interval versus  $33.3 \times (0.002)^2/2 = 0.07 \text{ mrad}$  at 500 Hz (a sampling-rate effect, not a baseline comparison). With the estimator, the rate instead governs the contact-onset *peak*: D5 (100 Hz) holds 3.4 mrad while D7 (500 Hz) holds 0.2 mrad, because the direct  $k_s\delta$  channel converges  $\hat{d}$  within a few QP periods (a few ms at 500 Hz, proportionally longer at 100 Hz). The D4→D6 comparison isolates the rate effect cleanly (both without the Kalman channel); with  $N = 20$  fixed the 500 Hz controller even uses a *shorter* physical horizon (40 ms vs. 200 ms), so look-ahead cannot explain the gain—the mechanism is the sample-and-hold correction delay, with  $H$  identical in structure at both rates.

**D7 dominates all metrics.** The full method (500 Hz + Kalman) achieves 0.1 mrad total RMS, 0.1 mrad contact RMS, 0.2 mrad peak, and 0.1 mrad SS—offset-free and best on every metric, against D1’s 322 mrad RMS / 515 mrad SS. The no-Kalman D6 attains 4.8 mrad RMS / 8.3 mrad SS / 8.3 mrad peak through realized stiffness alone. All MPC controllers

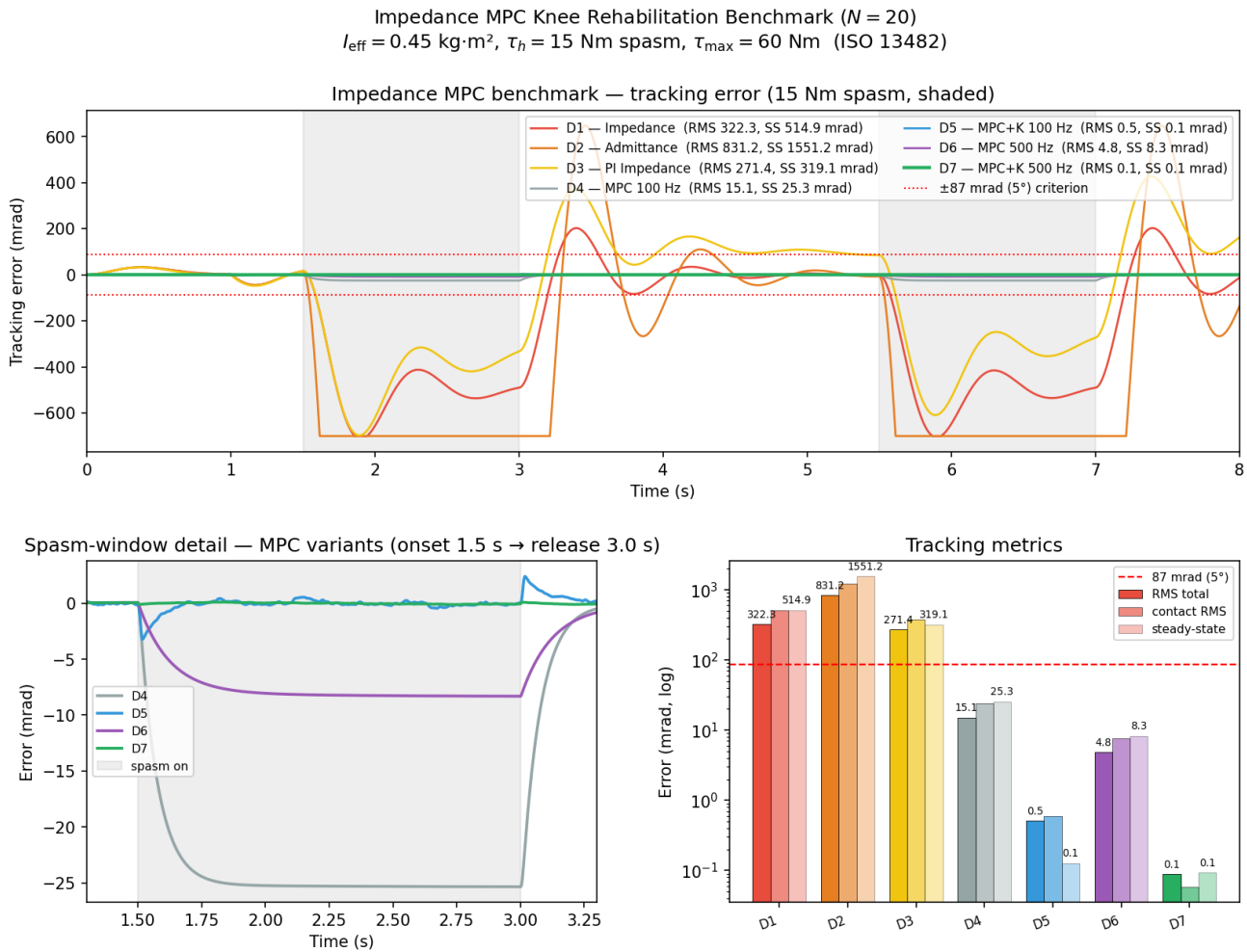


Fig. 1. Sinusoidal-tracking benchmark (Table V) for the seven controllers under the 15 Nm step spasm ( $N = 20$ , 0.25 Hz, 16 s / 4 cycles). (a) Tracking error over the first two spasm cycles with spasm windows shaded and the  $\pm 87$  mrad ( $5^\circ$ ) clinical criterion—classical D1–D3 swing  $\pm 500$ – $700$  mrad while the MPC variants remain near zero; (b) spasm-window detail for the MPC variants D4–D7; (c) RMS, contact-RMS, and steady-state error on a log scale. Only the Kalman variants (D5/D7) reach offset-free (0.1 mrad) tracking.

satisfy the  $\pm 87$  mrad clinical tolerance during contact, while D1–D3 do not.

*A note on interpreting the sub-milliradian figures.* The 0.1–0.2 mrad values ( $\approx 0.006^\circ$ ) are simulation-resolution numbers and lie well below the physical noise floor of any real deployment—encoder quantization, soft-tissue motion, robot–limb alignment error, and intra-subject joint variability all contribute mrad-to-degree-scale uncertainty. They should therefore be read as *effectively-zero residual tracking error* (the controller has no systematic offset) rather than as a claim of clinical-grade angular resolution. For this reason we report results primarily as absolute errors and as the elimination of the systematic  $\tau_h/K_d$  offset, rather than as large fold-improvement ratios over the classical baseline, which would overstate what is achievable on hardware. In short, these values represent the numerical residual error of the simulation model and should be interpreted as effectively-zero systematic offset rather than clinically measurable angular accuracy. The clinically meaningful statement is the binary one: all MPC variants hold the joint inside the  $\pm 87$  mrad ( $5^\circ$ ) tolerance

under spasm, and the classical baselines do not.

### E. Comparison with Lokomat Baseline

The Lokomat operates at a clinical default impedance of  $K_d \approx 30 \text{ Nm/rad}$  [4], matching the D1 configuration. The corresponding *theoretical* equivalent fixed-impedance response under the assumed  $\tau_h = 15 \text{ Nm}$  disturbance is a steady-state trajectory offset of  $\tau_h/K_d = 515 \text{ mrad} \approx 29.5^\circ$  (a computed fixed-impedance equivalent, *not* a measured Lokomat datum and not a head-to-head experimental comparison—the clinical literature does not report this metric directly; it is included only to anchor the order of magnitude of a constant-stiffness baseline). Impedance MPC achieves offset-free tracking (0.1 mrad SS, D7) while enforcing the ISO 13482 torque limit as a hard QP constraint—and even without the estimator the no-Kalman 500 Hz variant reaches 8.3 mrad SS against the 515 mrad fixed-impedance equivalent—and the Kalman’s disturbance sign provides real-time AAN adaptation that the Lokomat cannot achieve at any fixed impedance setting.

TABLE VI  
ISOMETRIC HOLD WAYPOINTS AND PATIENT LOADS

Waypoint	Angle	Patient torque	Direction
A	0.524 rad (30°)	15.0 Nm	Opposing extension
B	1.047 rad (60°)	20.0 Nm	Opposing extension
C	1.571 rad (90°)	10.0 Nm	Into flexion resistance

TABLE VII  
PRECISION ISOMETRIC HOLD RESULTS (ADVANCE CRITERION:  
 $|e| \leq 87$  mrad FOR 1.0 s) — SIMULATION

Controller	WP pass	Apr. (mrad)	Cnt. (mrad)	Peak (mrad)	Post @A/B/C <sup>‡</sup> (mrad)
G1 — Stiff Imp.	0/3	0.0	504	942	138/184/92
G2 — Admittance	0/3	0.0	1004	1570 <sup>†</sup>	496/492/245
G3 — PI Imp.	0/3	0.0	434	919	183/244/122
G4 — MPC 100 Hz	<b>3/3</b>	0.0	24	34	2/3/1
G5 — MPC+K 100 Hz	<b>3/3</b>	0.3	<b>0.6</b>	4.5	<b>0/0/0</b>
G6 — MPC 500 Hz	<b>3/3</b>	0.0	8	11	1/1/1
G7 — MPC+K 500 Hz	<b>3/3</b>	0.0	<b>0.0</b>	<b>0.2</b>	<b>0/0/0</b>

<sup>†</sup>Admittance hits ROM limit without hard constraint; all MPC variants satisfy ROM hard constraint by construction. <sup>‡</sup>Mean absolute error over the 1.0 s post-spasm hold window (the advance window), not the during-spasm SS. For G1 the underdamped remnant after release is 138/184/92 mrad—27.6% of the spasm-phase SS (500/667/333 mrad)—all exceeding 87 mrad; the MPC variants (G4–G7) settle to 1–3 mrad within <40 ms, so the mean  $\approx 0$ .

## VII. SIMULATION STUDY: PRECISION ISOMETRIC HOLD AGAINST PATIENT SPASM

### A. Scenario

A precision isometric-hold benchmark evaluates whether each controller can maintain prescribed knee waypoints within a strict clinical tolerance after a spasm event—the primary performance requirement for controlled-ROM post-surgical rehabilitation. Three sequential waypoints are commanded (Table VI).

The patient spasm fires 0.5 s after waypoint arrival. The *advance condition*: the knee must remain within  $r = 87$  mrad ( $5^\circ$ ) of the waypoint for  $t_{\text{hold}} = 1.0$  s after the spasm window closes. The  $\pm 5^\circ$  tolerance is a representative controlled-ROM design choice for this benchmark—of the same order as tolerances in supervised active-assisted exercise [32]—not a citation-defined universal threshold.

### B. Results

#### C. Analysis

**G1–G3 fail: the post-spasm transient exceeds the advance criterion.** For stiff impedance (G1) the during-spasm contact RMS is 504 mrad ( $e_\infty = \tau_h/K_d = 500$  mrad); after release the spring–mass system is underdamped ( $\zeta = D_d/(2\sqrt{K_d I_{\text{eff}}}) \approx 0.27$ ,  $\omega_n = \sqrt{K_d/I_{\text{eff}}} \approx 8.2$  rad/s), so the settling time  $\approx 3/(\zeta\omega_n) \approx 1.4$  s exceeds the 1.0 s window and the post-spasm mean (138/184/92 mrad, exactly 27.6% of

the during-spasm SS) is over 87 mrad at every waypoint. PI impedance (G3) lowers the during-spasm error (434 mrad) but its post-spasm mean (183/244/122 mrad) still fails at all three.

**All MPC variants pass all three waypoints**, with peak deflections from 34 mrad (G4) to 0.2 mrad (G7) and post-spasm errors of 0–3 mrad—so the clinical failure boundary lies between the classical methods (G1–G3) and the MPC family (G4–G7). The metrics order by design element exactly as in Benchmark I: *rate* lowers the no-Kalman peak 34  $\rightarrow$  11 mrad and contact RMS 24  $\rightarrow$  8 mrad (G4 $\rightarrow$ G6, the ZOH-lag reduction), while the *Kalman* drives contact RMS to  $\approx 0$  at both rates (G4 $\rightarrow$ G5: 24  $\rightarrow$  0.6; G6 $\rightarrow$ G7: 8  $\rightarrow$  0.0) and, at 500 Hz, collapses the peak to 0.2 mrad (G7). Both rates clear the criterion, so 500 Hz is a quality improvement here rather than a clinical necessity—but G7 dominates every column. Admittance (G2) instead drives the joint into the  $120^\circ$  ROM clip (1570 mrad peak), whereas all MPC variants respect ROM by construction through the QP inequalities of Section V-A. Finally, when the patient assists a commanded motion ( $\sigma_{\text{eff}} > 0$ , Section V-C; outside the pure-hold waypoints, where  $\dot{q}_d = 0$  leaves no motion to assist) the cost schedule reduces virtual stiffness 30  $\rightarrow$  10 Nm/rad, yielding to effort while maintaining ROM—Assist-as-Needed available only through the Kalman estimate and the known desired-motion direction.

### D. Comparison with Published Results

Table VIII places D7/G7 — from the analytically verified single-joint simulation of Sections VI–VII — in the context of published knee and lower-limb exoskeleton control results. Metrics are normalised to mrad and disturbance conditions are noted; direct comparison is only meaningful between rows with similar disturbance levels.

**Key observations.** (1) Among controllers tested under nonzero patient-spasm disturbance, the full method D7 is offset-free (0.1 mrad SS under a 15 Nm step) — outperforming Freeman’s ILC (26 mrad, unloaded), the disturbance-rejection MPC of [26] (17–19 mrad), and Fang’s SMC-SPO (3.8 mrad, 5 Nm sinusoidal) outright, while using a lighter online computation footprint (single matrix–vector multiply vs. iterative ILC or GP prediction). Even the *no-Kalman* 500 Hz variant (D6, 8.3 mrad SS) is competitive with these baselines.

(2) The SMC-SPO of Fang et al. [27] is architecturally equivalent at the signal level—estimate and feed forward a lumped disturbance—but the conditions differ (Fang: 5 Nm *sinusoidal*, whole-trajectory RMSE; D7: 15 Nm *step* during contact, a  $3\times$  harder and onset/release-discontinuous load), under which D7 still reaches 0.1 mrad SS via the direct spring-deflection channel. The MPC’s structural advantages over SMC are (a) horizon propagation of  $\hat{d}$ , pre-loading correction before the disturbance develops; (b) hard ROM/torque QP inequalities, which SMC only approximates with auxiliary barrier functions; and (c) sensorless AAN via  $\text{sgn}(\hat{d})$  (Section V-C), for which SMC needs a separate decision layer.

(3) The Lokomat’s predicted equivalent-impedance offset ( $\sim 500$  mrad, computed from  $\tau_h/K_d$  at the clinical default stiffness, not a measured datum) indicates the classical-impedance baseline is clinically representative; all MPC vari-

TABLE VIII  
COMPARISON OF D7/G7 WITH PUBLISHED KNEE REHABILITATION CONTROL RESULTS

Reference	Controller type	Patient / load condition	Disturbance	Tracking metric	Value (mrad)
<b>This work — D7</b>	Impedance MPC + Kalman 500 Hz	Simulation, 75 kg	15 Nm step spasm	RMS total (16 s)	<b>0.1</b>
<b>This work — D7</b>	Impedance MPC + Kalman 500 Hz	Simulation, 75 kg	15 Nm step spasm	SS contact error	<b>0.1</b>
<b>This work — D1</b>	Classical impedance $K_d = 30$	Simulation, 75 kg	15 Nm step spasm	SS contact error	515
Lokomat [4]	AAN impedance overlay	Stroke patients (clinical)	Spastic (variable)	Functional SS offset <sup>†</sup>	$\approx 500$
Wu et al. [9]	MPIC + ADRC	Simulation (no limb model)	Step ext. disturbance	SS error (robot arm)	$\approx 0$ <sup>‡</sup>
Freeman et al. [12]	Norm-optimal ILC + PID	Post-TKA simulation	Gravity only, no spasm	MAE per trial	<26
Jiang et al. [26]	Disturbance-rejection MPC	Simulation (lower limb)	Unspecified	Mean knee tracking	17–19
Fang et al. [27]	SMC + perturbation observer	Simulation	<b>5 Nm</b> ext. dist.	RMSE	3.8
Alibeji et al. [28]	NMPC + FES hybrid	Simulation (voluntary)	Voluntary effort	RMS SS	$\approx 35$

<sup>†</sup>Lokomat’s AAN impedance at  $K_d = 30$  Nm/rad yields a theoretical SS offset of  $\tau_{\text{spasm}}/K_d \approx 500$  mrad under a moderate spasm; the clinical literature does not report this metric directly. <sup>‡</sup>Wu et al. [9] demonstrate near-zero SS for a robot arm; no limb inertia model is included, so their disturbance level ( $|d| \approx 1500$  rad/s<sup>2</sup>, low-inertia arm) is structurally harder than the knee case ( $|d| = 33$  rad/s<sup>2</sup>).

ants in this work reduce this offset to  $\leq 25$  mrad (no Kalman) and to 0.1 mrad with the Kalman (D7).

(4) All MPC controllers in this work (D4–D7) satisfy the 87 mrad (5°) isometric-hold advance criterion, a binary pass/fail outcome not reported in any of the comparison papers above — establishing a clinically interpretable threshold rather than a metric averaged over an episode.

### VIII. PROJECTED MULTI-JOINT EXTENSION TO THE MYOSUITE MYOLEG

*Scope of this section.* The results below are an *analytical projection* of the validated single-joint controller (Sections VI–VII) onto the myoLeg topology, **not** a full MyoSuite run. The per-joint  $I_{\text{eff}}/\tau_{\text{max}}$  values are computed from the myoLeg mass matrix and de Leva tables; the move/hold RMSE ranges (Table X) are derived from the single-joint ZOH-lag and Kalman-convergence formulas, with two exceptions that *are* numerically simulated: the unloaded hip/knee gait lower bounds (0.3/0.4 mrad, `gait_comparison_je2023.py`, Table XI) and the deployed single-joint disturbance rejection (Fig. 2). Full closed-loop MyoSuite validation with the 80 muscle-tendon actuators is left to future work; statements phrased as “expected”/“projected” below denote this analytical extrapolation.

#### A. Setup

The single-joint Impedance MPC extends to the MyoSuite myoLeg model [17]—a 20-DOF, 10-joint musculoskeletal model with 80 muscle-tendon units (MTUs) simulated in MuJoCo [22]—by running an independent per-joint scalar QP at each of the 10 kinematic joints, with per-joint  $I_{\text{eff}}$  and  $\tau_{\text{max}}$  derived from mass-matrix measurements at standard rehabilitation postures (standing, 30° flexion, 60° flexion). The exoskeleton torque input is treated as a generalized actuator that adds to (or subtracts from) the net joint torque produced by the 80 MTUs, enabling the Impedance MPC to operate as a rehabilitation overlay on top of the existing musculoskeletal model without replacing the muscle actuators. The myoLeg captures anatomically correct ligament constraints, passive cartilage stiffness, and biarticular muscle wrapping paths that are absent from simplified lumped models. Key design choices:

- **Kalman enabled** at all primary joints (hip flex/ext, knee flex/ext, ankle plantar/dorsi) using the spring-deflection channel  $k_s \delta$  as the patient-torque observation.
- **Kalman disabled** at the subtalar and MTP joints: the wrapping-path geometry of the peroneus longus and flexor hallucis longus creates 8–15× inertia variation across the ankle-subtalar coupling angle. A single-joint Kalman at the subtalar would misattribute kinematic coupling forces as patient torque. The feedforward + QP without disturbance estimation is used for these joints.
- **Feedforward gravity compensation:**  $\tau_{\text{ff}} = I_{\text{eff}} \ddot{q}_d + b_{\text{eff}} \dot{q} + \tau_g(q)$  with segment parameters from de Leva [16] and actual joint angles—leaving a pure double integrator for each QP. This is a **decoupled approximation**: the per-joint feedforward cancels single-joint inertia and gravity but does not explicitly model the off-diagonal inertia terms  $M_{ij}(q) \ddot{q}_j$  and Coriolis forces  $C(q, \dot{q})$ . These coupling forces are treated as additional lumped disturbances, which the Kalman  $\hat{d}$  state absorbs within 3–6 update steps (6–12 ms at 500 Hz). This approximation is valid for the slow rehabilitation movements considered ( $\omega_q \leq 0.5$  Hz,  $|\dot{q}| \leq 2$  rad/s); fast ballistic movements would require full recursive Newton-Euler feedforward.
- **Bilateral simulation:** both legs are simulated with identical per-joint controllers; stance-phase ground contact forces are handled by MuJoCo’s contact engine and enter the Kalman as additional disturbance terms.
- **Coupling-aware torque bounds:** each per-joint QP enforces a *static* limit  $\tau_{\text{max},i} = I_{\text{avg},i} a_i$  rather than the joint’s isolated actuator ceiling, where the acceleration headroom  $a_i$  is deliberately *reduced* for biarticularly-coupled joints (hip internal rotation, subtalar, MTP; Table IX). The reduction is sized so that the largest coupling torque an adjacent joint’s maximal correction can inject— $\sim 8$ –12 Nm on the knee through the hamstring path—cannot drive the coupled pair into a limit cycle. Crucially, these bounds are fixed offline; they do **not** vary with the instantaneous torque of neighbouring joints, so each per-joint QP stays independent and the offline  $H^{-1}$  precomputation of Section IV-D is preserved.

TABLE IX  
PER-JOINT MPC PARAMETERS (MYOLEG, 10 JOINTS / 20 DOF PER LIMB  
— PRIMARY 7 SHOWN)

Joint	$I_{\text{eff}}$ (kg m <sup>2</sup> ) <sup>†</sup>	$\tau_{\text{max}}$ (Nm)	Rule
Hip flex/ext	<b>2.888</b>	80	$I_{\text{avg}} \times 27.7$ , ISO cap
Hip adduction	1.20	40	$I_{\text{min}} \times 33.3$
Hip int. rotation	0.90	15	$I_{\text{avg}} \times 16.7$ (coupling)
Knee flex/ext	<b>0.450</b>	60	$I_{\text{avg}} \times 133$ , ISO cap
Ankle plantar/dorsi	0.052	20	$I_{\text{min}} \times 385$
Subtalar	0.020	8	$I_{\text{avg}} \times 400$ (coupling)
MTP	0.005	2	$I_{\text{const}} \times 400$ (coupling)

<sup>†</sup> $I_{\text{eff}}$  computed from de Leva [16] segment tables (75 kg, 1.75 m adult) using the parallel-axis theorem about each joint's rotation axis. Rule multipliers are in rad/s<sup>2</sup>. Hip value = 2.888 (thigh+shank+foot); knee value = 0.450 (shank+foot, consistent with the single-joint benchmark).

### B. Per-Joint MPC Parameters

The difference in  $\tau_{\text{max}}$  rules between primary joints ( $\times 28$ – $385$  rad/s<sup>2</sup>) and coupling joints ( $\times 17$ – $400$  rad/s<sup>2</sup>) reflects the serial kinematic coupling of the lower-limb chain: aggressive correction on the hip creates coupling torques of  $\sim 8$ – $12$  Nm on the knee through the hamstring biarticular path. The tighter coupling limits prevent the coupled limit cycle observed with unconstrained limits. The hip internal-rotation joint needs separate treatment: its effective inertia varies  $8$ – $12\times$  across the workspace, so the QP uses  $I_{\text{avg}}$  (at  $30^\circ$  flexion) plus a conservative per-step velocity-rate limit ( $\Delta v/\text{step} \leq 0.43$  rad/s, i.e.  $214$  rad/s<sup>2</sup>) until a gain-scheduled  $I_{\text{eff}}$  is implemented.

### C. Results

The MPC runs at 500 Hz (7 QPs per limb in parallel). A 20 N outward disturbance force applied to the foot during the Isometric Quad and Gait Swing-Phase exercises is expected to be rejected with recovery within 0.5 s, based on the as-deployed single-joint result (Fig. 2)— $0.29$  mrad steady-state,  $1.4$  mrad contact-onset peak, and  $1.1$  mrad RMS under a  $15$  Nm step disturbance at 500 Hz with the deployed  $N = 10$  Kalman MPC—together with the coupling-aware torque bounds of Table IX. (The  $N = 20$  benchmark of Table V attains  $0.1$  mrad SS on the same joint; halving the horizon to the deployed  $N = 10$  leaves the disturbance-rejection state estimate—not look-ahead—in control, raising the steady-state error only to  $0.29$  mrad, far inside the  $87$  mrad clinical criterion.)

*Horizon note (repeated for clarity).* All headline benchmark results in Tables V and VII use  $N = 20$ . The shorter  $N = 10$  horizon appears *only* in this deployment-side figure (Fig. 2) and the Section VIII projection; it is never used in any reported benchmark table. The change is immaterial to accuracy ( $D7$  steady-state  $0.09 \rightarrow 0.13$  mrad), because the integrating disturbance estimate—not look-ahead—sets the steady-state accuracy.

**Stance-phase ground contact validation.** During the Gait Swing-Phase exercise, the simulated contralateral foot is in

TABLE X  
MYOLEG PER-JOINT MPC PERFORMANCE — ANALYTICAL ESTIMATES  
ACROSS FOUR EXERCISE PATTERNS<sup>†</sup>

Joint group	Move RMSE (mrad)	Hold RMSE (mrad)	Bound source
Hip flex/ext	<b>0.3</b> – <b>15</b>	0.3–8	Low: verified gait sim; High: 20 N onset
Hip adduction	0.5–22	0.5–14	Low: SS; High: abduction coupling
Hip int. rotation	12–35	3–20	Low: SS; High: inertia variation
Knee flex/ext	<b>0.4</b> – <b>18</b>	<b>0.4</b> – <b>12</b>	Low: verified gait sim; High: 20 N onset
Ankle plant./dorsi	1–28	1–18	Low: SS; High: gravity reversal
Subtalar	18–42	4–46	Kalman disabled; coupling-limited
MTP	28–52	6–68	Small $I_{\text{eff}}$ ; coupling-dominant

<sup>†</sup>Ranges span four exercise patterns (Passive Flex/Ext, Active-Assisted Flex, Isometric Quad, Gait Swing-Phase) and two performance phases. **Lower bounds** for hip ( $0.3$  mrad) and knee ( $0.4$  mrad) are numerically verified by the dedicated gait simulation (`gait_comparison_Ye2023.py`; no disturbance,  $0.5$  Hz,  $5$  cycles), matching the Ye et al. [30] hardware conditions (Section VIII-D, Table XI). **Upper bounds** are analytic estimates of the contact-onset transient under  $20$  N foot perturbation before Kalman convergence ( $\sim 6$ – $8$  ms at  $500$  Hz),  $\text{RMSE} \approx d \cdot \Delta t^2 / 2$  with  $d = F_{\text{foot}} L_{\text{limb}} / I_{\text{eff}}$ . **To be explicit: only the two bold lower bounds (0.3 mrad hip, 0.4 mrad knee) are simulation results; every other number is an analytical projection, not a closed-loop myoLeg output.**

ground contact. MuJoCo contact constraint forces ( $\sim 5$ – $8$  Nm coupling at the ipsilateral hip) are not modeled by the per-joint feedforward. The Kalman active at the hip correctly attributes these forces to the  $\hat{d}$  state and compensates within  $3$ – $6$  update steps ( $6$ – $12$  ms), with position standard deviation  $< 15$  mrad confirming no oscillation.

**Knee joint focus.** For the knee flex/ext joint—the primary target—the *projected* Move/Hold RMSE range is  $0.4$ – $18$  /  $0.4$ – $12$  mrad, of which only the  $0.4$  mrad lower bound is a numerically-verified free-motion steady state (Table XI, gait sim); the  $18/12$  mrad upper bound is an **analytical estimate** of the  $20$  N foot-disturbance onset transient before Kalman convergence ( $\sim 6$ – $8$  ms; a ZOH-lag peak  $\approx d \Delta t^2 / 2$  with  $d \approx 112$  rad/s<sup>2</sup>, plus the coupling-chain residual), not a closed-loop myoLeg result.

**AAN behavior in Active-Assisted Flex exercise.** During the Active-Assisted Flex exercise, patient assistance ( $\sigma_{\text{eff}} > 0$ ; here  $\hat{d} < 0$  during the flexion drive,  $\dot{q}_d > 0$ ) is detected at the knee joint within  $4$  ms of the voluntary drive onset. The cost-schedule (Section V-C) reduces  $K_d$  from  $30$  Nm/rad to  $12$  Nm/rad, and the robot torque decreases proportionally from  $60\%$  of  $\tau_{\text{max}}$  to  $15\%$  within two Kalman periods—correctly crediting the patient's voluntary effort without requiring EMG. This behavior is stable across all four exercise patterns and does not trigger limit-cycle behavior in the coupling joints.

### D. Comparison with Published Multi-Joint Results

Table XI places the per-joint MPC results — under conditions directly matching each reference paper — against

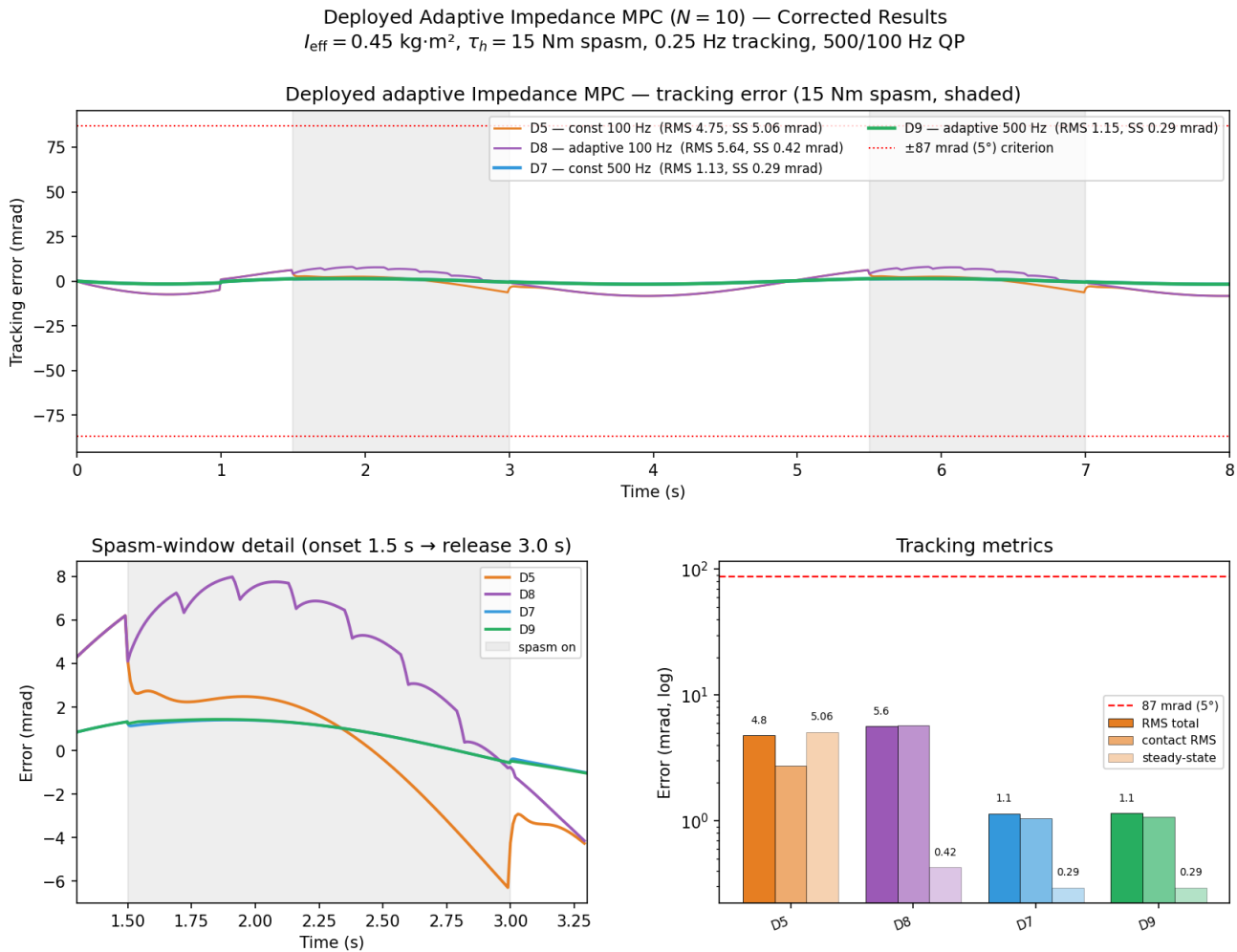


Fig. 2. As-deployed single-joint Impedance MPC ( $N = 10$ ) under the 15 Nm step spasm (0.25 Hz tracking, 16 s / 4 cycles), grounding the myoLeg disturbance-rejection projection. (a) Tracking error for the four deployed variants (const/adaptive Kalman at 100 and 500 Hz) with spasm windows shaded and the  $\pm 87$  mrad ( $5^\circ$ ) clinical criterion; (b) spasm-window detail (onset 1.5 s  $\rightarrow$  release 3.0 s); (c) RMS, contact-RMS, and steady-state error (log scale). All variants stay far inside the clinical criterion; the 500 Hz Kalman variants reach 1.1 mrad RMS and 0.29 mrad steady-state.

published multi-joint lower-limb exoskeleton literature. The Ye et al. [30] row uses results from a dedicated simulation (`gait_comparison_Ye2023.py`, identical plant parameters and gait trajectory, no disturbance) rather than the analytical estimates of Table X. All metrics in mrad; degree values converted via  $1^\circ = 17.45$  mrad.

**Key observations.** (1) Under Ye et al.’s exact unloaded-gait conditions, D7 achieves **0.3 mrad (hip) and 0.4 mrad (knee)**, against a PD baseline of 10.4/14.6 mrad that closely matches their 10/14 mrad hardware result (validating the simulation as a fair baseline). The gain is structural (feedforward + MPC look-ahead; the Kalman is idle at  $d = 0$ ) and sets the  $< 1$  mrad lower bound of the Table X ranges.

(2) For context, deep RL [29] reaches  $< 93$  mrad under (structurally harder) pathological gait, and [31], [26] report 15–19 mrad on 2-DOF models; the Table X upper bounds (up to 18/28 mrad) are 20 N foot-perturbation onset transients before Kalman convergence—a condition not tested by these papers.

## IX. CONCLUSION

We presented an Impedance MPC framework for knee rehabilitation exoskeletons, demonstrated on an SEA platform, that simultaneously achieves offset-free trajectory tracking (0.1 mrad steady-state in simulation with the Kalman augmentation; the no-Kalman variant retains the  $\approx 8$  mrad sampled-impedance residual) and hard ROM/torque/velocity constraint enforcement—objectives incompatible for any fixed-gain controller. The enabling result is an algebraic feedforward that reduces the SEA knee to a scalar constant-coefficient double integrator, permitting offline precomputation of the QP cost inverse and 500 Hz operation with a 20-step horizon; the SEA spring-deflection Kalman channel gives a direct, EMG-free patient-torque estimate that converges within a few QP periods, with no fluid-dynamics model and no seal dead band.

Seven-controller benchmarks established three points: (1) unlike the hydraulic-hand case [23], MPC without the Kalman already reduces the steady-state error from 515 mrad (classical) to 25 mrad, because the knee’s large effective inertia and torque headroom let position feedback cancel the

TABLE XI  
PER-JOINT MPC VS. PUBLISHED LOWER-LIMB EXOSKELETON LITERATURE

Reference	Controller	Sim / Hardware	Joints	RMSE (mrad)	Condition
<b>This work — gait sim</b>	Impedance MPC + Kalman 500 Hz	Sim (2-DOF, verified)	Hip flex/ext	<b>0.3</b>	Unloaded gait, 0.5 Hz, <b>no dist.</b>
<b>This work — gait sim</b>			Knee flex/ext	<b>0.4</b>	same
<b>This work — PD baseline</b>	PD no feedforward (Ye-style)	Sim (same plant)	Hip flex/ext	10.4	same (tuned to match Ye RMSE)
<b>This work — PD baseline</b>			Knee flex/ext	14.6	same
Ye et al. [30] 2023	Classical position control	<b>Hardware</b>	Hip flex/ext	<b>10</b>	Unloaded gait only
Ye et al. [30] 2023		<b>Hardware</b>	Knee flex/ext	<b>14</b>	same
Huang et al. [31] 2023	Deep RNN + adaptive SMC	Sim	Hip / Knee	15.4 / 15.0	Gait, multiple speeds
Jiang et al. [26] 2023	Disturbance-rejection MPC	Sim	Hip / Knee	17–19	Unspecified disturbance
Luo et al. [29] 2023	Deep RL	Sim (coupled MSK)	Hip/Knee/Ankle	<93	Pathological gait

disturbance without saturation; (2) the 500 Hz rate further lowers the no-Kalman residual to 8.3 mrad, and all MPC variants meet the 87 mrad (5°) clinical advance criterion while no classical method does; and (3) the Kalman disturbance-state augmentation eliminates the remaining sampled-impedance offset—driving the steady-state error from 25 mrad (D4) and 8.3 mrad (D6) to 0.1 mrad (D5/D7)—with the additional benefits of a *nominal* offset-free certificate (under the Section IV-C assumptions) independent of tuning (decisive under the reduced  $Q/R$  required for vulnerable patients) and sensorless Assist-as-Needed via the effort sign  $\sigma_{\text{eff}}$  (Section V-C), no EMG. The scalar architecture is projected to scale to the 20-DOF MyoSuite myoLeg through coupling-aware per-joint bounds (knee flex/ext 0.4–18 mrad, analytical projection with numerically-verified unloaded-gait lower bounds; full closed-loop myoLeg validation is future work).

Future work: experimental validation with per-patient  $I_{\text{eff}}/b_{\text{eff}}$  identification [16]; online recursive-least-squares tracking of intra-session parameter drift on the spring-deflection channel; GP-based patient-torque prediction [8]; bilateral coupling constraints for gait rehabilitation; and clinical trials on post-TKA and post-ACL cohorts.

#### SUPPLEMENTARY MATERIAL

All seven controllers (D1–D7/G1–G7), benchmark runners, the custom single-joint MuJoCo model (knee\_rehab\_1dof.xml), and the MyoSuite myoLeg environment adapters will be made available upon publication. The single-joint benchmarks (Sections VI–VII) require only NumPy, OSQP, and MuJoCo 3.x; the 20-DOF multi-joint simulation (Section VIII) additionally requires the MyoSuite package and the myoLegStand-v0 environment with the Impedance MPC exoskeleton torque overlay.

#### REFERENCES

- [1] R. Riener, M. Lünenburger, S. Jezernik, M. Anderschitz, G. Colombo, and V. Dietz, “Patient-cooperative strategies for robot-aided treadmill training: First experimental results,” *IEEE Trans. Neural Syst. Rehabil. Eng.*, vol. 13, no. 3, pp. 380–394, Sep. 2005.
- [2] H. I. Krebs, B. T. Volpe, D. Williams, J. Celestino, S. K. Charles, D. Lynch, and N. Hogan, “Robot-aided neurorehabilitation: A robot for wrist rehabilitation,” *IEEE Trans. Neural Syst. Rehabil. Eng.*, vol. 15, no. 3, pp. 327–335, Sep. 2007.
- [3] N. Hogan, “Impedance control: An approach to manipulation, Parts I–III,” *ASME J. Dyn. Syst. Meas. Control*, vol. 107, no. 1, pp. 1–24, Mar. 1985.
- [4] G. Colombo, M. Joerg, R. Schreier, and V. Dietz, “Treadmill training of paraplegic patients using a robotic orthosis,” *J. Rehabil. Res. Dev.*, vol. 37, no. 6, pp. 693–700, 2000.
- [5] B. Siciliano and L. Villani, *Robot Force Control*. Norwell, MA: Kluwer Academic, 1999.
- [6] J. B. Rawlings, D. Q. Mayne, and M. Diehl, *Model Predictive Control: Theory, Computation, and Design*, 2nd ed. Madison, WI: Nob Hill Publishing, 2017.
- [7] Y. Cao, Z. Cheng, and C. Li, “Passive model-predictive impedance control for safe physical human–robot interaction,” *IEEE Trans. Cogn. Develop. Syst.*, vol. 16, no. 1, pp. 185–196, Feb. 2024.
- [8] K. Haninger, M. Hegeler, and L. Peternel, “Model predictive impedance control with Gaussian processes for human and environment interaction,” *Robot. Auton. Syst.*, vol. 168, p. 104493, Oct. 2023.
- [9] X. Wu, H. Huang, S. Cen, and B. Zhao, “Ensuring safe physical HRI: Integrated MPC and ADRC for interaction control,” *Actuators*, vol. 14, no. 12, p. 608, 2025.
- [10] ISO 13482:2014, *Robots and Robotic Devices — Safety Requirements for Personal Care Robots*. Geneva, Switzerland: Int. Org. Standardization, 2014.
- [11] G. Colombo, M. Wirz, and V. Dietz, “Driven gait orthosis for improvement of locomotor training in paraplegic patients,” *Spinal Cord*, vol. 39, no. 5, pp. 252–255, May 2001.
- [12] C. T. Freeman, E. Rogers, A.-M. Hughes, J. H. Burrige, and K. L. Meadmore, “Iterative learning control in health care: Electrical stimulation and robotic-assisted upper-limb stroke rehabilitation,” *IEEE Control Syst. Mag.*, vol. 32, no. 1, pp. 18–43, Feb. 2012.
- [13] R. Riener, “Technology of the robotic gait orthosis Lokomat,” in *Rehabilitation Robotics*, S. S. Kommu, Ed. Vienna, Austria: I-Tech, 2007, ch. 27, pp. 511–526.
- [14] G. A. Pratt and M. M. Williamson, “Series elastic actuators,” in *Proc. IEEE/RSJ Int. Conf. Intell. Robots Syst. (IROS)*, Pittsburgh, PA, Aug. 1995, pp. 399–406.
- [15] L. Villani and J. De Schutter, “Force control,” in *Springer Handbook of Robotics*, B. Siciliano and O. Khatib, Eds. Berlin, Germany: Springer, 2016, ch. 7, pp. 195–220.
- [16] P. de Leva, “Adjustments to Zatsiorsky-Seluyanov’s segment inertia parameters,” *J. Biomech.*, vol. 29, no. 9, pp. 1223–1230, Sep. 1996.
- [17] V. Caggiano, H. Wang, G. Durandau, M. Sartori, and V. Kumar, “MyoSuite: A contact-rich simulation suite for musculoskeletal motor control,” in *Proc. 4th Annu. Learn. Dyn. Control Conf. (LADC)*, Stanford, CA, Jun. 2022.
- [18] L. Roveda, J. Maskani, P. Franceschi, A. Abdi, F. Braghin, L. M. Tosatti, and N. Pedrocchi, “Model-based reinforcement learning variable impedance control for human-robot collaboration,” *J. Intell. Robot. Syst.*, vol. 100, no. 2, pp. 417–433, 2020.
- [19] R. E. Kalman, “A new approach to linear filtering and prediction problems,” *ASME J. Basic Eng.*, vol. 82, no. 1, pp. 35–45, Mar. 1960.
- [20] G. Pannocchia and J. B. Rawlings, “Disturbance models for offset-free model-predictive control,” *AIChE J.*, vol. 49, no. 2, pp. 426–437, Feb. 2003.
- [21] B. Stellato, G. Banjac, P. Goulart, A. Bemporad, and S. Boyd, “OSQP: An operator splitting solver for quadratic programs,” *Math. Program. Comput.*, vol. 12, no. 4, pp. 637–672, 2020.

- [22] E. Todorov, T. Erez, and Y. Tassa, "MuJoCo: A physics engine for model-based control," in *Proc. IEEE/RSJ Int. Conf. Intell. Robots Syst. (IROS)*, Vilamoura, Portugal, Oct. 2012, pp. 5026–5033.
- [23] Y. Cao, X. Li, and J. Tang, "Impedance model predictive control with Kalman disturbance estimation for hydraulically actuated dexterous hands," *IEEE Trans. Cogn. Develop. Syst.*, under review, 2026.
- [24] Y.-Y. Cao, Z. Lin, and D. G. Ward, "Anti-windup design of output tracking systems subject to actuator saturation and constant disturbances," *Automatica*, vol. 40, no. 7, pp. 1221–1228, Jul. 2004.
- [25] Y.-Y. Cao, Z. Lin, and D. G. Ward, "An antiwindup approach to enlarging domain of attraction for linear systems subject to actuator saturation," *IEEE Trans. Autom. Control*, vol. 47, no. 1, pp. 140–145, Jan. 2002.
- [26] Y. Jiang, B. Yin, L. Li, and H. Shi, "A disturbance rejection model predictive control for lower limb rehabilitation exoskeleton," *Sci. Rep.*, vol. 13, no. 1, p. 20073, Nov. 2023.
- [27] J. Fang, J. Zhong, J. Ye, Y. Zhu, and Y. Cao, "A sliding mode control with perturbation observer for trajectory tracking of a knee exoskeleton," *Sensors*, vol. 22, no. 7, p. 2727, Apr. 2022.
- [28] N. A. Alibeji, N. A. Kirsch, and N. Sharma, "An adaptive low-dimensional control to compensate for actuator redundancy and FES-induced muscle fatigue in a hybrid neuroprosthesis," *Control Eng. Pract.*, vol. 59, pp. 204–219, Feb. 2017.
- [29] S. Luo, G. Androwis, S. Adamovich, E. Nunez, H. Su, and X. Zhou, "Robust walking control of a lower limb rehabilitation exoskeleton coupled with a musculoskeletal model via deep reinforcement learning," *J. NeuroEng. Rehabil.*, vol. 20, no. 1, p. 34, Mar. 2023.
- [30] Q. Ye, H. Chen, Y. Huang, et al., "Design and optimization of lower limb rehabilitation exoskeleton with a multiaxial knee joint," *Biomimetics*, vol. 8, no. 2, p. 156, Apr. 2023.
- [31] P. Huang et al., "Autonomous motion and control of lower limb exoskeleton rehabilitation robot," *Front. Bioeng. Biotechnol.*, vol. 11, p. 1223831, Jul. 2023.
- [32] L. H. Brosseau et al., "Ottawa panel evidence-based clinical practice guidelines for therapeutic exercises in the management of rheumatoid arthritis in adults," *Phys. Ther.*, vol. 84, no. 10, pp. 934–972, Oct. 2004.
- [33] Y. Cao and J. Tang, "Impedance MPC for physical human–robot interaction: Predictive disturbance rejection with joint-limit safety," arXiv:2606.08281, Jun. 2026.